Eidgenössische Technische Hochschule Zürich
Swiss Federal Institute of Technology Zurich

Coupling an acoustic resonator to a superconducting qubit using an improved flip-chip bonding process

Semester thesis

Laurent Michaud

michaudl@student.ethz.ch

Laboratory for Solid State Physics
Hybrid Quantum Systems Group
ETH Zürich

Supervisors:
Uwe von Lüpke
Prof. Dr. Yiwen Chu

July 21, 2020

Acknowledgements

I'm thankful for the support of my group and the availability of my supervisors. Special thanks to Yu Yang, a group member who helped me by performing ANSYS numerical simulations for the project. The bonding agent transfer process was suggested by Cao Xiabao, a member from the ETH microfluidic group during a meeting kindly set up by Prof. deMello. I'm also grateful to Andreas Stucker, Walter Bachmann, Willy Staubli and the teams from the mechanical workshop and the engineering office who assisted me in the various engineering tasks presented in this report. I express my gratitude towards the BRNC operation team, particularly to Roland Germann, Ralph Heller, Ronald Grundbacher, Ute Drechsler. I would also like to thank the FIRST operation team as well as Dirk van Swaay for sharing his expertise on PDMS and SU-8 manufacturing.

Abstract

A computing device taking advantage of quantum-mechanical phenomena such as superposition or entanglement is called a quantum computer. Richard Feynman conjectured in 1982 [1] that a quantum computer could simulate the dynamics or static properties of another quantum system. This assertion was proven to be true in 1996 [2]. Experimental realizations of quantum computers succeeded in approaching problems that were known to be intractable if implemented on classical devices [3]. This gain of control over quantum systems has been used for a variety of applications. From the measurement of gravitational waves using squeezed states of light [4] to the use of entangled quantum states to provide safer communication channels [5].

Quantum bits (qubits) are 2-dimensional quantum systems, they are the building blocks of quantum computers. A plethora of quantum systems can be used to instantiate qubits [6, 7, 8]. One of the most successful implementations of qubit has been developed in circuit quantum electrodynamics (cQED). The field of cQED focuses on coupling light and matter in artificial systems defined lithographically. Qubits created in cQED are instantiated in bidimensional millimeter-sized geometric features. To reach the quantum regime, these features are cooled down to exhibit superconducting properties. Therefore cQED qubits are often called superconducting qubits. Quantum computers based on this kind of qubit were able to implement sophisticated quantum algorithms [9]. These results were made possible thanks to a global effort to improve superconducting qubits architectures. For instance, the coherence time of superconducting qubits was increased by 6 orders of magnitude over the past two decades [10]. These endeavors are still ongoing as better qubits are required to run more complex and useful algorithms[11].

Rather than improving solely cQED architectures, hybrid quantum circuitry can alleviate the limitations of superconducting qubits by coupling them with other quantum systems. In this paradigm, quantum systems suffering from different kinds of limitations are coupled to exhibit novel properties [12]. Acoustic cavities have recently been brought in this field. The high quality factor and small mode volumes of these acoustic device make them suitable for quantum memories [13]. Acoustic cavities can be coupled to other quantum systems (NV centers, quantum dots, ions, superconducting qubits, ...) by the means of piezoelectric, piezomagnetic, and photostrictive effects who respectively couple the electric field, magnetic field and electromagnetic field to acoustic modes [14]. More specifically, this project is based on a hybrid system presented in Ref.[15, 16] where a superconducting qubits is coupled to an acoustic cavity using the piezoelectric effect. Reaching the strong coupling regime is an emblematic milestone in this field.

In the paper by Chu et al. [17], strong coupling is reached by fabricating a superconducting qubit and a bulk acoustic wave resonator on distinct chips of sapphire. The two chips are bonded together in a flip-chip bonding (FCB) process, allowing the electric field of the superconducting qubit to permeate a layer of piezo-electric material and thereby coupling it to the mechanical resonator. The performance of the hybrid system relies on the accuracy and reproducibility of the bonding. Using minimal quantities of bonding agent is also important as it impacts the coherence of the qubit through dielectric losses. In this report, we present a new bonding process granting a micrometric alignment precision by the use of an industrial flip-chip bonder. The use of a microcontact printing technique [18] allows precise deposition of sub-nanoliter amounts of a bonding agent.

Contents

Chapter 1

Introduction

This project is dedicated to the elaboration of a new flip-chip process for the hybrid quantum system presented in ref.[17]. This hybrid architecture is made of a 3D transmon qubit and a high-overtone bulk acoustic wave resonator. Each of these systems is built on distinct sapphire chips. The present section introduces their working principles as well as the coupling mechanism enabling their mutual interaction.

1.1 3D transmon qubit

One of the first kinds of qubit built with a superconducting circuit is known as the Cooper pair box (CPB) [19]. The main constituents of this system are sketched on fig.1.1. The circuit makes use of a Josephson junction [20] placed between a superconducting island and a reservoir of electrons.

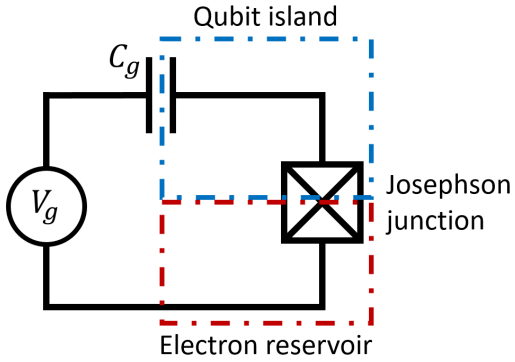

Figure 1.1: A Cooper pair box consists of a superconducting island connected to a superconducting electron reservoir through a Josephson junction. The electrons are transferred from the electron reservoir to the qubit island due to a voltage source V_g connected to the qubit island by a gate capacitance C_g.

A voltage source is capacitively-coupled to the qubit island to control the number of Cooper pairs inside the latter. Cooper pairs are the natural charge carriers in superconductors [21]. The creation process of these pairs requires an amount of energy labeled $E_{\text{Cooper pair}}$*. Operating the superconducting circuit at a temperature $T < E_{\text{Cooper pair}}/k_B$ with k_B the Boltzmann constant, prevents thermal fluctuations from breaking Cooper pairs. $E_{\text{Cooper pair}}$ being on the order of 10^{-3} eV [22], the temperature needs to be well below 10K†. The total capacitance of the qubit island to the rest of the system is $C_\Sigma = C_g + C_j$ with C_g the gate capacitance and C_j the Josephson junction capacitance. The Coulomb energy $E_C = (2e)^2/2C_\Sigma$ defines the energy of a Cooper pair on the island for a zero gate voltage. If $E_{\text{Cooper pair}} \gg E_C$, we can consider that all the electrons in the qubit island are paired. The remaining

*$E_{\text{Cooper pair}}$ corresponds to the energy gap in a superconductor taking into account the interaction between the Cooper pairs. The binding energy of an isolated Cooper pair is much smaller (5 orders of magnitudes) and is not relevant for the study of a superconductor as these pairs are present in high density[22]

†This estimate is valid for a BCS superconductor.

degree of freedom of the qubit island is the number of excess Cooper pairs n that tunneled from the electron reservoir to the qubit island thought the Josephson junction. The CPB works by preventing spontaneous tunneling of the Copper pair to the qubit island. This is done by operating the system in a regime where $E_C \gg E_J$ where E_J is the energy barrier a Cooper pair has to overcome to tunnel in the junction. The operator can enable a single tunneling by changing the gate voltage. The transition energy between the states $n = 0$ and $n = 1$ is $\Delta E = E_C(1 - 2n_g)$ where n_g is the dimensionless gate voltage $n_g = C_g V_g/(2e)$. Because Josephson junctions behave as non-linear inductors, the CPB can be seen as a non-linear LC oscillator. As a consequence, the energy levels are not equally spaced. For instance, the transition energy between $n = 1$ and $n = 2$ will be $\Delta E + \alpha$ where α is the anharmonicity parameter. In theory, this enables the manipulation of the two lowest energy states ($n = 0$ and $n = 1$) without leakage to the other states ($n > 1$). This result justifies the fact that a CPB can be used to instantiate a qubit. In an experimental setup, the noise generated by the fluctuation of the charge is called Q_{residual} and comes from the junction imperfection which shifts the value of n_g by $Q_{\text{residual}}/(2e)$. This limits the coherence time of the CPB by changing the transition energy between states. To alleviate this limitation, the sensitivity to charge noise can be reduced significantly by operating the system in a regime where $E_C \ll E_J$ at the expense of reducing $|\alpha|$. This is called the transmon regime [23]. In this project, a superconducting qubit in the transmon regime is used. To make its transition frequency tunable, we use a SQUID* loop made of two Josephson junctions. The operator can change the qubit's frequency by the means of an external coil generating a magnetic field that modifies the flux across the SQUID loop.

To interact with the qubit and change its state, we use microwave signals. The signals are sent through coaxial cables. They are injected in a micromachined cavity by coupling pins [25]. The cavity can be made of aluminum or copper. The microwave signal will get coupled to a transverse electromagnetic mode (TEM) of the cavity. The use of a 3D cavity provides an electromagnetic environment free of spurious modes. As a consequence, radiation losses are strongly suppressed and the coherence time of the qubit is improved. Fig. 1.2 from ref.[25] shows the 3D cavity, the coupling pin slot as well as the shape of the electric and magnetic field lines of TEM101 and its corresponding surface current.

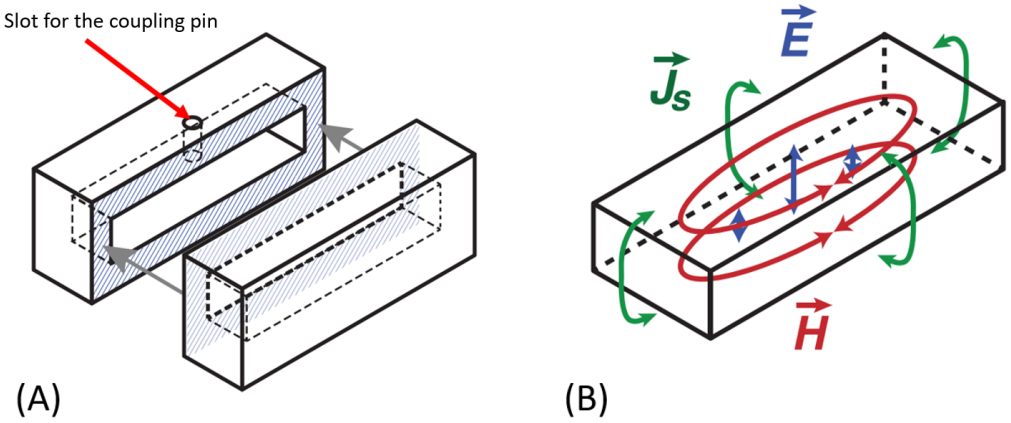

Figure 1.2: From [25],(A) The micromachined cavity consists of two parts that are screwed together. A coupling pin (placed in its appropriate slot) allows the generation of TEMs. (B) Electric and magnetic field lines of TEM101 and the corresponding surface current.

Fig. 1.3 shows the cavity used in the current setup. The transmon qubit is embedded inside the 3D microwave cavity. It is anchored in a clamping rail by small indium bits. These bits also serve as a heat bridge to thermalize the qubit to the cavity.

*stands for superconducting quantum interference device, see ref.[24]

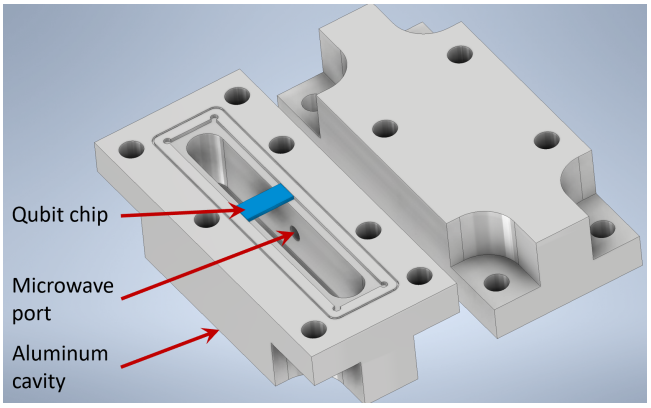

Figure 1.3: The qubit chip is clamped inside a cavity made of aluminum or copper (top and bottom parts are shown here). A microwave port allows signals from a coaxial cable to couple to the box and qubit modes inside the cavity.

The qubit chip is sketched on fig.1.4. Two capacitors pads are linked by a pair of Josephson junctions. As will be explained in the next part, the bulk acoustic resonator has a disc of piezoelectric material. To improve the coupling between the superconducting qubit and the disc of piezoelectric material, a circular shaped antenna is built on the qubit's chip and connected to one of the pads. These features are made by depositing a layer of aluminum of less than a hundred nanometers on a sapphire chip.

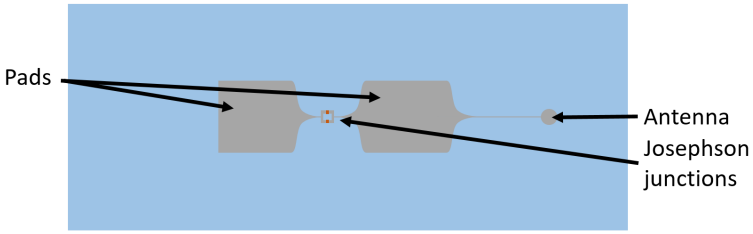

Figure 1.4: The qubit chip consists in a pair of pads linked by a Josephson junction, an antenna is also connected to one of the pads to transfer the qubit state to the other chip

1.2 High-over tone bulk acoustic wave resonator

As outlined in the abstract, hybrid quantum circuitry is a very rich field of research. A variety of quantum systems can be coupled to superconducting qubits such as quantum dots, Rydberg atoms, surface acoustic waves, and mechanical systems [12]. Using acoustic cavities instead of electromagnetic cavities is motivated by several reasons. For instance, acoustic cavities are more compact than their electromagnetic counterparts. This is because the speed of sound in crystalline structures is 4 orders of magnitude smaller than the speed of light in vacuum. So for a given operating frequency, the light's wavelength will be 4 orders of magnitude bigger than the sound's wavelength [26]. In this project, we use a high-overtone bulk acoustic wave resonator (HBAR). High-overtone explicitly states that the resonator is designed to operate at gigahertz frequencies. An architecture enabling the creation of such a resonator is reported in ref.[15] by Chu et al. It is of great interest to understand its working principle and its limitations since the device used in this report is a direct improvement of the latter. Fig.1.5 from ref.[15] shows the actual device.

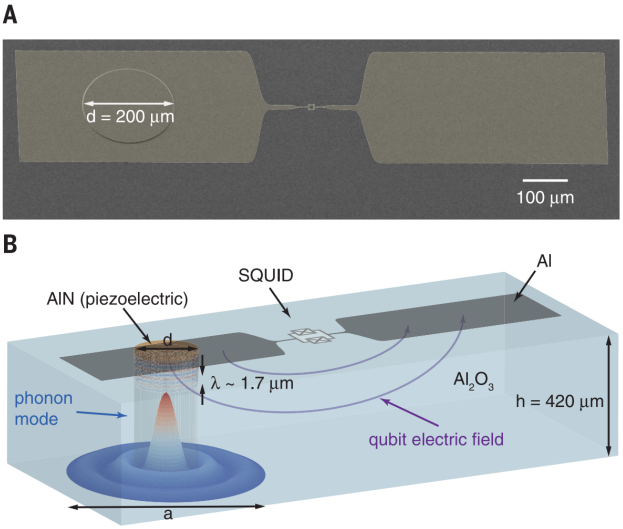

Figure 1.5: Hybrid quantum system reported in ref.[15]. A superconducting qubit is coupled to a bulk acoustic wave resonator. A: A 200 µm diameter disc of piezoelectric material (aluminum nitride) is placed on top of the superconducting qubit. B: A phonon mode is generated in the bulk of a sapphire chip, under the disc of piezoelectric material activated by the electric field of the qubit.

The parallel faces of a sapphire chip can be seen as acoustic mirrors that reflect the sound waves propagating in the bulk of the crystal. By using special symmetry axis of the crystal, it can shown [15] that the sound modes are the same as the electromagnetic modes in a Fabri-Pérot cavity. The sound modes of the acoustic cavity are coupled to the electric field of the qubit's pads through a disc made of piezoelectric material (PM) located on the pad's surface. An important concept arising in the context of coupled quantum systems is strong coupling regime. Strong coupling means that we can transfer a quantum state from one system to another within a period of time smaller than the individual decay rates of each subsystem. It can be formalized by writing $g \gg \max(\kappa, \gamma)$ [27] where g is the coupling strength, κ and γ the depolarization exponential decay rates of the qubit and the acoustic resonator respectively. In ref.[15], strong coupling regime was reached and the coherent transfer of quantum states between the superconducting qubit and the bulk acoustic resonator was reported. Sapphire is a crystalline structure with a low defect density, making it suitable for constructing acoustic resonators with high quality factors. For instance, the resonator from ref.[15] has a quality factor around 7.1×10^5, in the range of typical values for acoustic devices (one order of magnitude higher than a typical surface acoustic wave resonator coupled to a qubit [28]).

In a more recent paper by Chu et Al. [17], the architecture of the system was drastically changed. The qubit and acoustic resonator sit on separate sapphire chips which are then assembled in a flip-chip geometry. This simplifies the fabrication procedure and allows the quality check of each system before the assembly. Fig.1.4 shows a qubit chip very similar to the one used in ref.[17]. A circular antenna radiates the qubit's electric field. The resonator chip is designed such that the PM faces the qubit's antenna. The resonator chip surface facing the qubit chip has a microlens. This is sketched on fig.1.6 and the dimensions of the hybrid system are shown in fig.1.7. The microlens creates a plano-convex geometry that is capable of selecting stable, transversely confined acoustic modes. This is a clear improvement compared to the Fabry-Pérot geometry previously implemented in ref.[15]. Another important requirement is to selectively couple the qubit to a single cavity mode. This is achieved by the plano-convex resonator which can control the frequency spacing between the transverse modes. The PM constitutes the extreme part of the microlens (the green domains in fig.1.6 and 1.7). The qubit's antenna is tailored to generate a strain profile in the PM that matches the fundamental Gaussian transverse modes of the acoustic resonator.

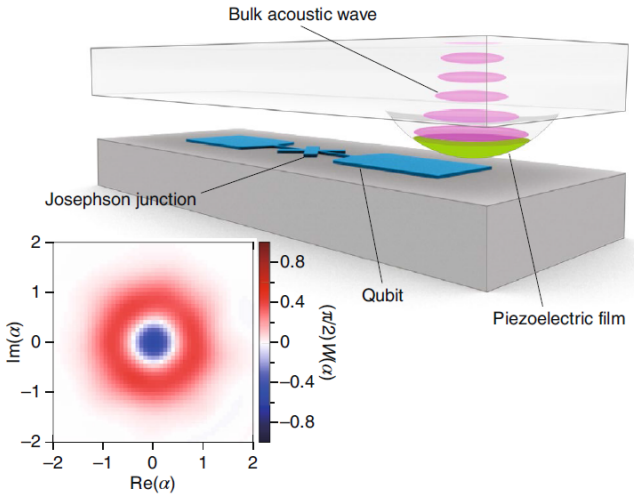

Figure 1.6: Scheme from ref.[27] shows a flip-chip geometry used in the context of hybrid quantum circuitry. The qubit chip and the resonator are placed on distinct chips facing each other. The microlens of the resonator is partially made of a piezoelectric material allowing the coupling between these systems. The lower inset shows the Wigner function corresponding to a single-phonon Fock state of the acoustic cavity. The former was obtained by performing state-tomography on the device engineered in ref.[17].

Fig.1.7 presents in more details the flip-chip geometry. We can see that the inter-chip distance is fixed by spacers. These features are made of aluminum. They are built on the top of auxiliary microlenses that are fabricated together with the microlens facing the qubit's antenna. Using this technique, the spacer's height will directly control the distance between the tip of the microlens and the qubit's antenna[†]. The chips are locked into position by placing drops of cryogenic glue (GE varnish) on the sides (the yellow domains on fig.1.7).

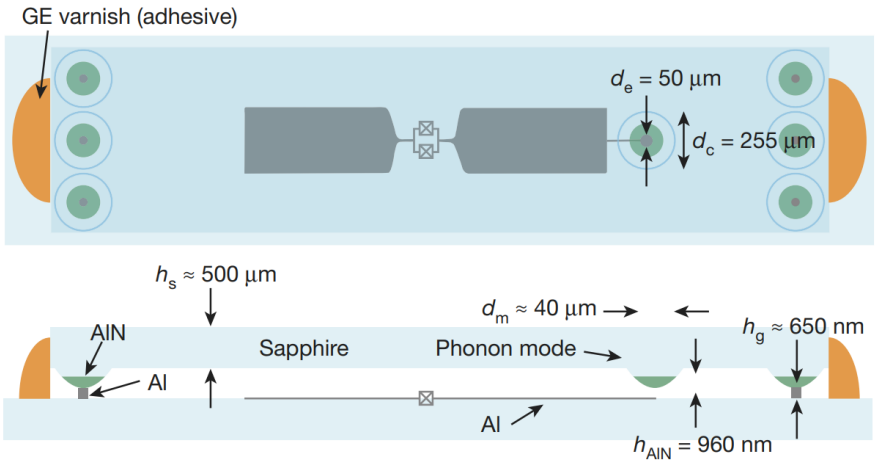

Figure 1.7: Detailed scheme from ref.[17] of the flip-chip geometry used in [17]. The chip containing the acoustic resonator has 6 identical microlenses on its edges. Aluminum spacers are deposited on them. Their thickness is h_g but the actual distance between the qubit's antenna and the central microlens may be larger owing to imperfections in the flip-chip assembly. Other quantities are the diameters of the qubit's antenna d_e, the width of the microlens d_c and the acoustic-mode waist d_m, along with the thicknesses of the piezoelectric (aluminum nitride) element constituting the tip of the lens h_{AlN} and sapphire substrate h_s.

[†]the actual distance may be higher if some particles are trapped between the spacers and the qubit chip during the flip-chip assembly

1.3 Sensitivity of the coupling factor depending on the accuracy of the FCB

Having understood the working principles of the transmon qubit and the HBAR, we new focus on the coupling mechanism between them and its sensitivity regarding the misalignment of the chips. This will be helpful to assess the performance of the bonding process elaborated in this report. It will be useful to elaborate on the bonding process as we need to quantify how precise the alignment should be.

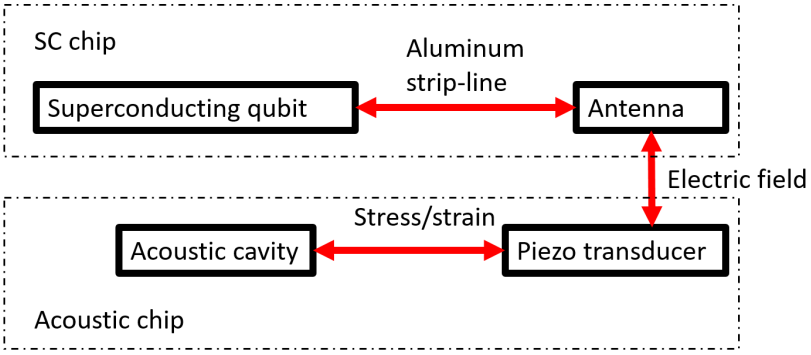

Figure 1.8: Transduction scheme used in the hybrid quantum system discussed in this report. The superconducting qubit is connected to an antenna. The latter radiates an electric field that permeates through a piezo element located on the acoustic chip. Sound modes are then generated inside the acoustic chip by the piezo element. This transduction chain is bidirectional [17].

Fig.1.8 summarizes the transduction scheme. The electric field radiated by the qubit's antenna has three spatial components. Each of these can induce different kinds of strain in the PM resulting in longitudinal or transverse acoustic waves in the bulk of the chip. The strain vector* describing the deformations in the solid assumes the form: $\vec{S} = (S_x, S_y, S_z, S_{yz}, S_{xz}, S_{xy})$. S_i describes normal strains where the deformation is an expansion or compression along the axis $i = x, y, z$. S_{ij} corresponds to shear strains in the plane including the i and j axis. The former kind of strain generates longitudinal waves in the bulk of the chip whereas the latter generates shear waves. In the same manner, the stress vector $\vec{T}$ describes differents types of forces acting on the surfaces of the solid. Stress and strain are linked by the relation $\vec{T} = c\vec{S}$ known as the generalized Hooke's law with c the stiffness tensor. The c tensor is a linear map between two 6 dimensional vectors. The piezoelectric tensor d is a 6×3 matrix quantifying the properties of a material to manifest strain due to electric field $\vec{S} = d\vec{E}$. To obtain the stresses induced by the antenna's electric field, we use the Hooke's law: $\vec{T} = c\vec{S} = cd\vec{E}$. The energy E_{elastic} stored in the PM is given by a volume integral :

$$E_{\text{elastic}} = -\int T(\vec{x})S(\vec{x})\mathrm{d}V \tag{1.1}$$

To simplify the study, we assume the electric field in the vicinity of the PM to be mainly along the z-axis. The strain vector becomes $S = (0, 0, S_z, S_{yz}, S_{xz}, 0)$. Besides, only the longitudinal wave generation is considered. Thus, there is only one component of interest:$S_z(\vec{x}) = dE_z(\vec{x})$. In this specific case, relation 1.1 takes the following form:

$$E_{\text{elastic}} = -c_{33}d_{33}\int E_z(\vec{x})S(\vec{x})\mathrm{d}V \tag{1.2}$$

Quantizing the electric and the strain fields allows to identify the elastic energy with the exchange energy of the Jaynes-Cumming model [15]:

*using the Voigt notation to represent the strain and stress tensors

$$-E_{\text{elastic}} = \hbar g = c_{33} d_{33} \int E_z(\vec{x}) S(\vec{x}) \mathrm{d}V \tag{1.3}$$

Now that we have derived the equation for the coupling factor g, it becomes clear that to maximize g, we should match the profile of the electric field along the z-axis to the strain profile of the acoustic mode we are targeting. It can be shown that the acoustic eigenmodes of a plano-convex geometry are Hermite-Gauss as shown in ref.[29]. These modes are identical to the ones found in an optical cavity and are also called TEM (Transverse Electromagnetic Modes). To simplify the study, we will focus on the TEM00 which is Gaussian. The electric field produced by the qubit's antenna should then also have a Gaussian profile. The antenna we fabricate on our qubit chip is disc-shaped, the same design as the one used in ref.[17]. To better understand why the profile of the electric field produced by a disc-shaped antenna is Gaussian we use a numerical simulation. We focus on the profile of the electric field located on a virtual line passing in the middle of the antenna. This line is then moved along the normal axis of the antenna to study the evolution of the profile. To compute the electric field, we need to know the charge distribution σ of a disc of radius R. Using ref.[30], we find that $\sigma(\vec{r}) = \frac{Q}{4\pi R\sqrt{R^2-|\vec{r}|^2}}$ for $|\vec{r}| < R$ and $\sigma = 0$ otherwise. Fig.1.9 shows that the profile of the electric field converges towards a Gaussian as we move away from the antenna's surface. To quantify this convergence, the goodness of a Gaussian fit is reported for each profile. Fig.1.10 shows the accumulation of the charges around the contour of the antenna.

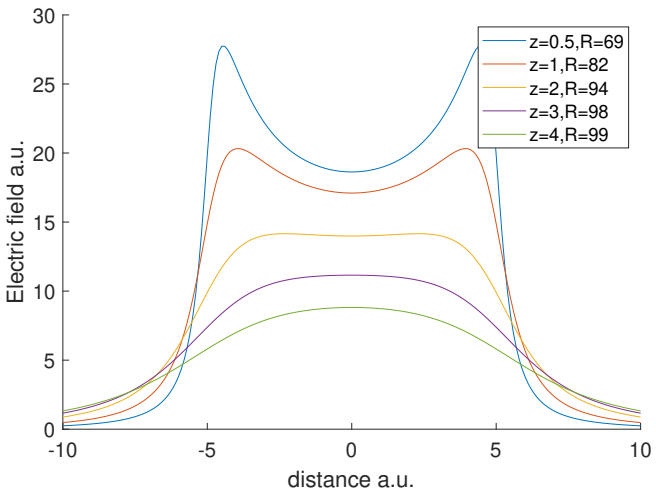

Figure 1.9: Profile of the electric field generated by a charged disc. The field is measured along a line passing by the middle of the disc and moved along the normal axis of the disc by an amount z. The goodness $R[\%]$ of a Gaussian fit computed for each profile is reported.

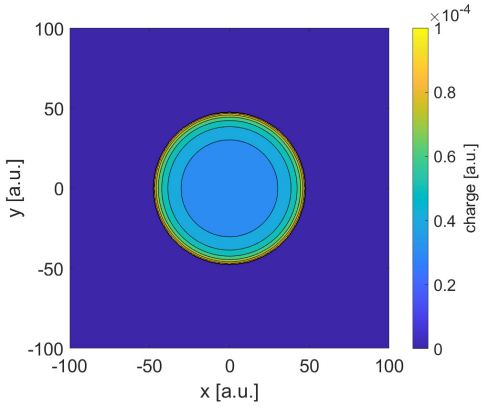

Figure 1.10: Charge distribution of a disk, the charges accumulates on the boundaries of the disk.

In the following, we assume the shape of the electric field to be perfectly Gaussian. Because of the rotational symmetry, we can restrict the study along a single axis. Along the x axis passing through the middle of the antenna, we can write the following equations for the electric and strain fields:

$$E_z(x) \propto e^{-\left(\frac{x-\mu_E}{\sigma_E}\right)^2} \qquad S(x) \propto e^{-\left(\frac{x-\mu_S}{\sigma_S}\right)^2}$$

where σ_E, σ_S are the variances of the electric and strain fields while μ_E, μ_S are their mean values.

With these functions, eq.1.3 becomes a one-dimensional integral of Gaussian distributions product:

$$\hbar g = c_{33} d_{33} \int_{-\infty}^{\infty} e^{-\left(\frac{x-\mu_E}{\sigma_E}\right)^2} e^{-\left(\frac{x-\mu_S}{\sigma_S}\right)^2} \mathrm{d}x \tag{1.4}$$

The integration variable can assume all the values along the real axis: $x \in]-\infty, \infty[$. This simplifies the integration and is a valid assumption if the Gaussian profiles are well localized inside the shape

of the piezoelectric material σ_E,$\sigma_s \ll d_{\mathrm{AlN}}$. After completing the square of the exponent, we obtain the dependency of the coupling factor g with respect to the misalignment $\Delta\mu = \mu_E - \mu_S$ of the two Gaussian profiles:

$$g \propto \frac{\sigma_E \sigma_S}{\sqrt{\sigma_E^2 + \sigma_s^2}} \exp\left(-\frac{\Delta\mu^2}{\sigma_E^2 + \sigma_S^2}\right) \tag{1.5}$$

A reasonable objective for the quality of the alignment is a maximal reduction of the coupling factor by 5 percents after the bonding. This criteria can be written as follow:

$$g = g_0 \exp\left(-\frac{\Delta\mu^2}{\sigma_E^2 + \sigma_s^2}\right) = 0.95 g_0$$

Solving this equation for $\Delta\mu$ gives:

$$\Delta\mu = \sqrt{\sigma_E^2 + \sigma_s^2}\sqrt{-\ln 0.95}$$

The width of the acoustic mode generated in the real HBAR device is 47 µm while the variance of the electric field is approximately 40 µm. Using these values, we have a bound for the maximal misalignment value, $\Delta\mu < 14.4$ µm. It should be pointed out that the electric field plotted in figure 1.9 is only valid in the electrostatic case. In our system, the qubit's operating frequency is in the gigahertz range. And electrodynamics simulation is more suited for an accurate study of the hybrid system. We can compare these two approaches. The hybrid system is simulated with a finite element solver called ANSYS HFSS. The inter-chip distance is fixed at 10 µm while the radius of the qubit's disc-shaped electrode is set to 55 µm. Once the electric field of the antenna has been simulated, we extract its profile at the surface of the acoustic chip. We integrate this profile with a Gaussian profile representing a strain profile having a variance of 47 µm. The Gaussian strain profile is shifted by an amount $\Delta\mu$ to study the impact of the misalignment. Fig.1.11 shows the relative change of g predicted by eq.1.5 and by the numerical approach we have described. The numerical simulation gives a higher upper bond for the misalignment. With our 5 percents loss threshold for g, $\Delta_{\mathrm{num}}\mu = 22$ µm.

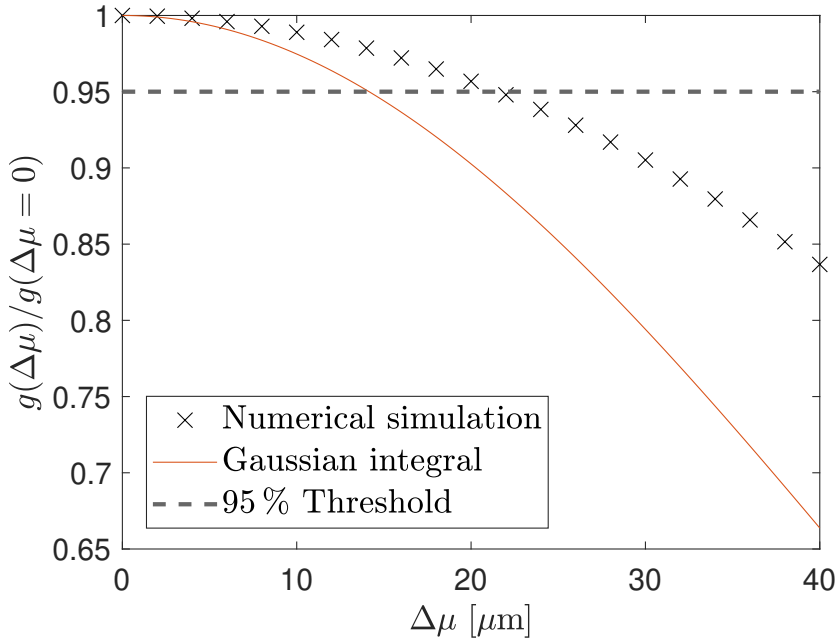

Figure 1.11: The theoretical computation predicts a higher sensitivity regarding the misalignment than the numerical approach. The simulation is done for an inter-chip distance of 10 µm

Chapter 2

Flip-chip bonding process

In the introductory chapter, we saw that thanks to the use of a novel hybrid quantum system architecture called flip-chip geometry, several properties of the quantum system were improved, like the coherence time and the mode selectivity of the HBAR. This chapter is split into three parts. The first will introduce the basics concepts of flip-chip architecture and how we are using it for our system. The second will show how the flip-chip bonding was performed in ref.[17]. The last part will present the new flip-chip bonding procedure.

2.1 Introduction

Flip-chip bonding (FCB) is a widely used technique in integrated circuit (IC) industry. It gives access to a new kind of chip architecture by allowing the bonding of two chips on top of each other (one facing up and the other down hence the name flip-chip). Most of the FCBs in the IC industry are galvanic, meaning that a current can flow between the chips through a soldering bump. In our case, the two chips interact via capacitive coupling. The bonding material can thus be an insulator. The hybrid quantum system we are constructing thought the FCB should fulfill several criteria listed below.

1. The thermal expansion coefficients of the two chips should match. Otherwise, the chips would shrink differently during the cool-down and it would induce shearing forces that might break the bonding bumps.

2. The system is operated at less than a Kelvin. Only one of the two chips is in thermal contact with the 3D-cavity shown in figure (1.3) (which is thermally bridged to the Helium dilution system). The other chip is thermalized through the soldering bumps. These need to be designed accordingly to the time one is willing to wait for the cool-down of the system.

3. The assembled chips should remain bonded together even if the whole assembly is flipped.

4. As the transmon radiates an electric field, it is important to minimize dielectric losses as much as possible. The bonding agent should be placed in amounts as small as possible and as far away from the qubit as possible.

The first criterion is fulfilled by the use of sapphire substrates for both chips. The second and third criteria are opposed to the forth one. The quantity of bonding agent we use in this process is chosen to guarantee mechanical stability while reducing dielectric losses. We now present the main characteristics of an FC bonding setup. As shown in fig.2.1, a total of 6 degrees of freedom (DOF) [31] needs to be controlled while manipulating two chips, some with more accuracy than others depending on the alignment setup. Two chip holders are required for the bonding operation. They grab and hold chips in place. The holders' mobility can be allocated differently, see section 2.2 and

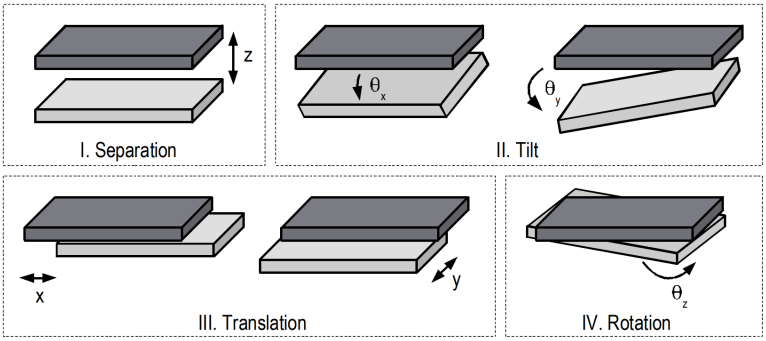

Figure 2.1: Scheme extracted from ref.[31]. 6 degrees of freedom describe the alignment of the chips. I) The separation along the z axis. II) Two tilting angles θ_x and θ_y. III) Two translations along the x and y axis. IV) Rotation along the z axis.

For the alignment, an optical instrument like a microscope or a numerical microscope can be used. Alignment marks located on both chips are then matched under the point of view of the microscope.

2.2 Starting ground for the design of the FCB

In the paper by Chu et al. [17], the FCB was achieved using the setup shown in fig.2.2. It consists of a chip clamp mounted on a rotating holder for θ_z correction, see fig.2.1. The upper chip is held by a bent needle with a droplet of liquid polymer. The needle is mounted on a 3-axis micro-stage, see fig. 2.3. This flexible holder is designed to deform if too much stress is applied to the upper chip. This may happen if the inter-chip distance is underestimated by the operator during the bonding. The two holders can adjust 4 degrees of freedoms and we saw that for an FCB, a total of 6 degrees of freedom exists. The tilting angles θ_x and θ_y are adjusted by the approach mechanism. When the operator reduces the separation z, the upper chip spacers make contact with the lower chip and correct the tilting angles.

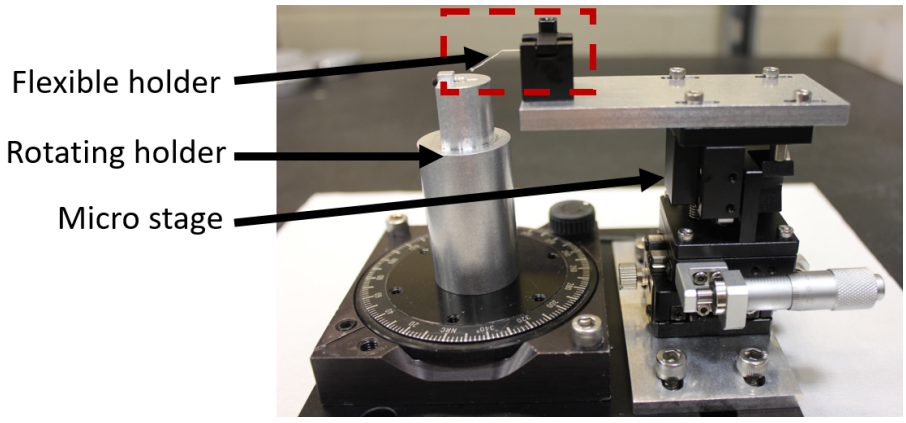

Figure 2.2: Setup to perform the FCB used in ref.[17]. Details about its use are given in the text. The dashed red frame shows where the two chips are located, more details are shown on fig.2.3

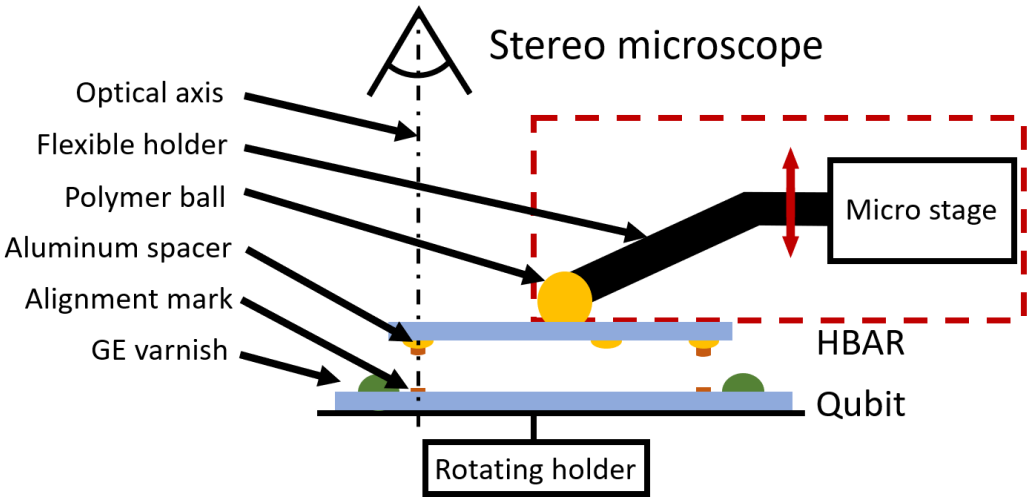

Figure 2.3: Detailed view of the alignment setup shown in fig.2.2. Its working principle is described in the text.

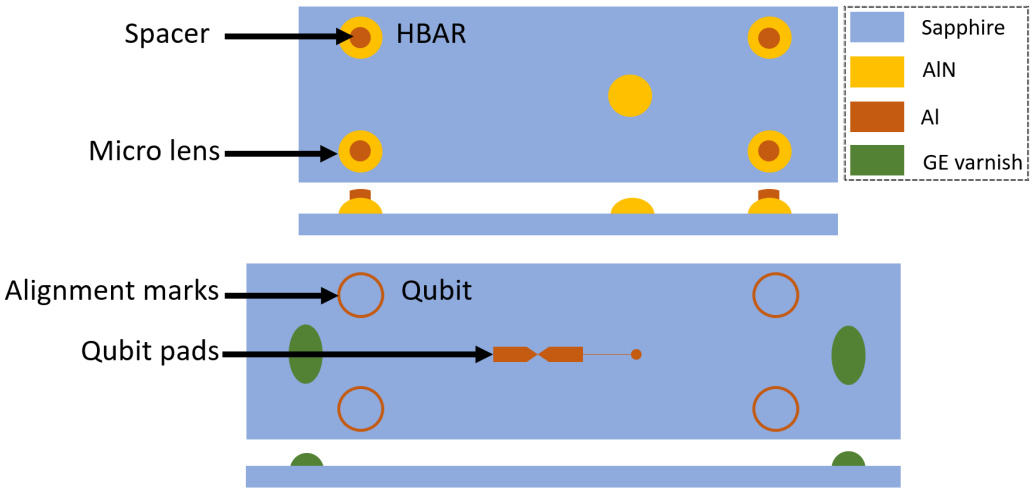

Figure 2.4: Simplified sketch of the chip architecture used in [17]. Aluminum spacers built on the top of the microlenses on the HBAR chip are opaque to optical light, making them naturally suitable for alignment purposes. The qubit chip has ring shaped aluminum patterns as alignment marks. GE varnish drops are added on the sides of the qubit chip to complete the bonding.

A stereo microscope* is then used to align the chips. The aluminum spacers built on the lenses of the HBAR chip are used in combination with aluminum ring patterns on the qubit chip as alignment marks, see fig.2.3,2.4. When using a stereo microscope, we cannot resolve both substrates, this limitation is the main motivation for the use of a circular pattern, it gives a good accuracy even if one of the two alignment components is not focused, see fig.2.5.

*a long working distance microscope

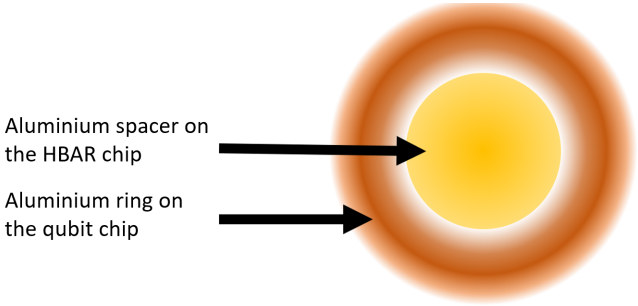

Figure 2.5: The simplicity and identifiable character of circle-shaped alignment marks helps to mitigate the fact that the operator cannot focus both substrates with a the stereo microsope

To make sure that the chips are aligned when the operator matches the alignment marks, the optical axis needs to be perpendicular to the surface of the chips, see fig.2.3. This condition is fulfilled by making sure that the alignment setup and the stereo microscope lie flat on the same surface. The rotating holder has a clamping surface machined to have a horizontal plane. The upper chip being weakly attached to the other holder isn't lying at a comparable precision in a horizontal plane. Having a setup able to check and correct the parallelism of the holders would be a desirable feature. After iterating alignment corrections along the xy plane and in the θ_z axis, the chips are placed in close contact. With the help of a micropipette, a cryogenic glue (for example GE varnish) is added on the sides of the qubit chip as shown on fig.2.3,2.4. The bonding is executed in the next tens of seconds to prevent the glue from drying. The separation between the chips after the bonding is about 4 µm meaning that a drop of 0.1 µL spreads on a disk of 2.8 mm radius. This has an impact on the coherence of the qubit since its electric field passes through the glue which has a dielectric loss much greater than sapphire. In the next chip architecture, the dimensions of the chips will make impossible the use of the sides for the bonding, see fig.2.6.

2.3 Presentation of the new FCB

In this section, we describe the new FCB. Firstly, we start by summarizing the updated designs of the chips. Secondly, we show how we have customized and used an industrial chip bonder for the flip-chip assembly. Thirdly, we detail the choice and the transfer of the bonding agent.

2.3.1 Updated designs of the qubit and HBAR chips

As we plan to implement a more accurate method for the bonding agent deposition, the design of the chips is modified. Fig.2.6 shows as side cut view of the 3D cavity used in this project and presented on fig.1.3. We see that there is no room left for the bonding agent drops on the side of the qubit chip[†]. Instead, we plan to place small drops of bonding agent directly between the chips. The spacing mechanism is also modified. Previously, we were evaporating aluminum micro-pillars on auxiliary microlenses to set the spacing between the top of the central lens and the qubit's antenna, see section 1.2. Now we set the inter-chip distance by fabricating micro-pillars made of photoresist on the surface of the HBAR chip. The recipe for these spacers is detailed in appendix A.

[†]as it was the case in ref.[17], see fig.1.7)

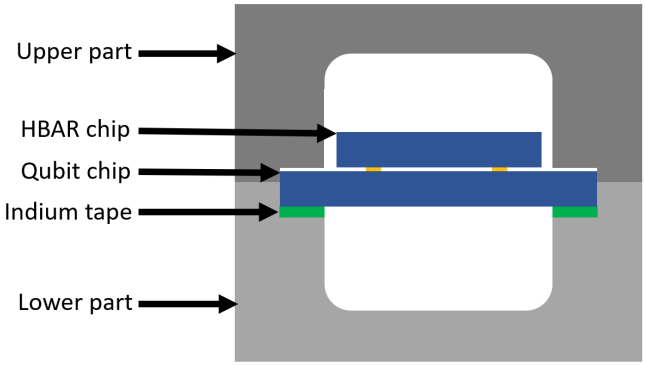

Figure 2.6: Side cut of the 3D cavity shown on fig.1.3. Indium tape is used to maintain the qubit chip in place. The mechanical stability and the thermalization of the HBAR chip is ensured by the size of the bonding bumps.

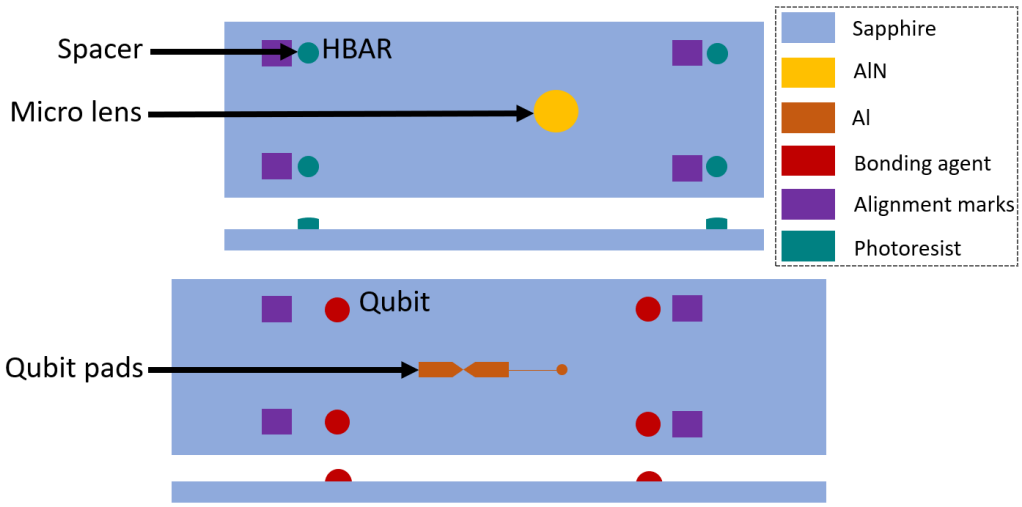

Figure 2.7: New designs for the HBAR (3 mm by 5 mm) and qubit (3 mm by 7 mm) chips. The spacers are made of photoresist, the alignment marks are more sophisticated. The bonding agent is located closer to the electric field of the qubit.

As will be explained in the next section, the new chip bonder allows the operator to focus both chip surfaces. Meaning that we can use more sophisticated alignment marks called Vernier pattern. This will improve the alignment precision and also enable the direct measure of the misalignment between the chips after the bonding. These alignment marks are described in the context of flip-chip bonded devices in ref.[32]. These marks are complementary rulers, each chip has a ruler made of rectangular features spaced by S_1 and S_2 respectively, see fig.2.8. If the chips are aligned (up to the resolution of the Vernier pattern), the reference features (framed by the dashed rectangle on fig.2.8) are matched, if the n-th pair of rectangular features are matching, the misalignment is $n|S_1 - S_2|$.

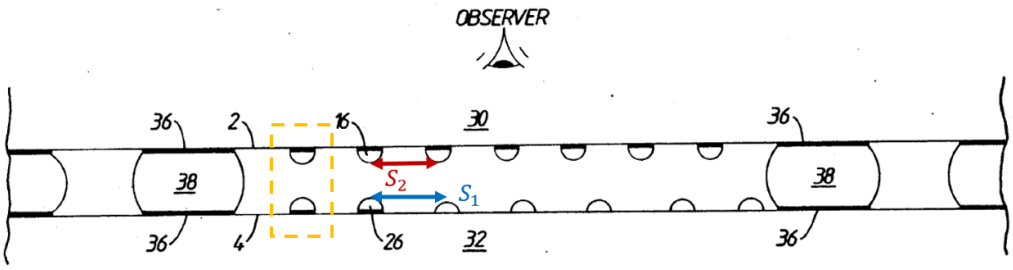

Figure 2.8: Side cut view of chips equipped with Vernier pattern from ref.[32]. Vernier patterns consist of two complementary rulers. Their different spacings S_1 and S_2 help the observer to measure the misalignment. The resolution of the pattern is |S2-S1|. If the reference features framed by the dashed rectangle are matched, the chips are aligned up to the resolution of the Vernier pattern equal to $S_1 - S_2$.

2.3.2 Chip bonder SET FC150

A major advance in the precision of the bonding is made by using an industrial grade chip bonder engineered by SET[‡] called FC150. This machine is specially designed to align and bond chips. It consists of two kinds of holders. The lower one called the *chuck* can rotate along its normal axis and translate in the xy plane. The upper holder called the *arm* only translates along the z-axis. Both holders are equipped with vacuum pipes to grab chip holding tools. This feature allows the user to tailor his bonding process by fabricating his own holding tools. These can be designed according to the chip dimensions. Fig.2.9 shows the two main parts. The FC150 has a numerical microscope mounted on rails next to the alignment stage. Its resting position does not prevent the arm to go into contact with the chuck. To align the chips, the microscope moves between the chuck and the arm, see fig. 2.10.

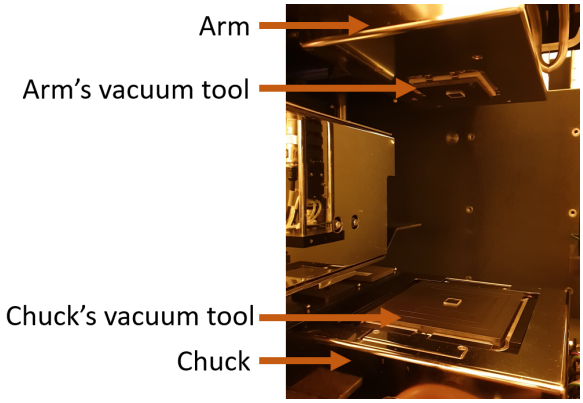

Figure 2.9: The FC150 includes a chuck and an arm. The former can rotate along its normal axis and translate along x and y while the latter moves exclusively along the z axis (after the calibration).

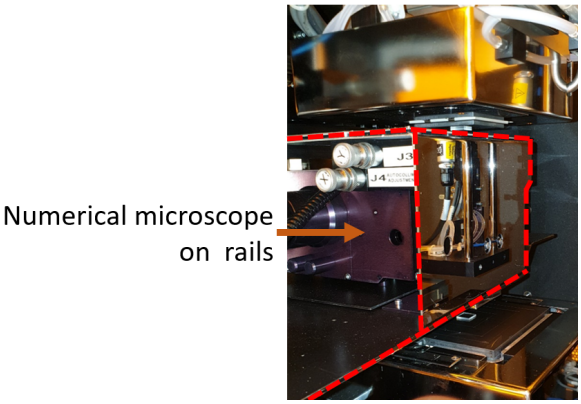

Figure 2.10: A numerical microscope can slide between the chuck and the arm for the alignment step

Once the microscope is inserted, the arm and chuck can move along the z-axis to focus both chips. Fig.2.11 shows the output of the microscope when two chips are aligned with complementary vernier patterns, this situation is sketched on fig.2.12.

[‡] http://www.set-sas.fr/en/pp422408-421389-FC150.html

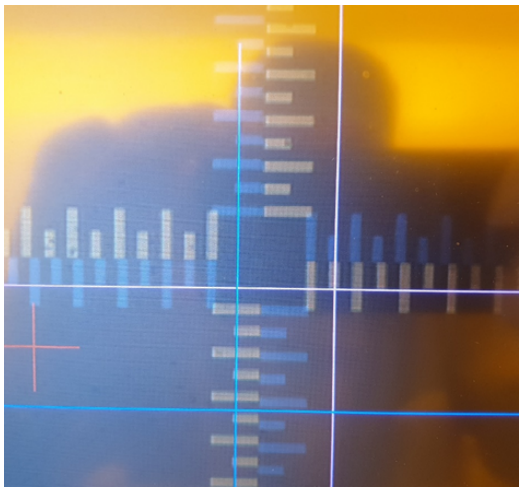

Figure 2.11: Vernier patterns are used for the callibration test of the FC150. The microscope colors the upper and lower chips differently to ease the alignment.

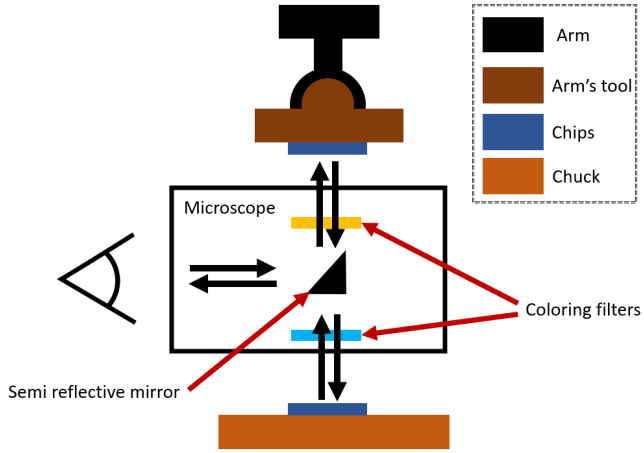

Figure 2.12: The microscope contains a semi-transparent mirror allowing to redirect the light coming from the upper and the lower chip. Colouring filters help to distinguish the two inputs. When working on a single chip, the microscope can shut off the other input to ease the reading.

Fig.2.13 gives an overview of the elements surrounding the chuck. While to bottom chip is placed in the chuck, the upper chip has to be grabbed by the arm. The operator does not directly perform this task, he rather places the upper chip on a substrate designed to hold the upper chip which is called a *cassette*. The arm can then grab the upper chip by lowering the arm's tool position until making contact with the chip. Cassettes can be clamped on the 3 by 2 grid of cassette slots located on the left of the chuck. Behind, a tool bay presents 5 slots for the arm's tools to rest on. On the right, a lower chip holder is loaded by default. It is made to fit the dimensions of practice chips, used to test and train the alignment procedure. An auxiliary vacuum tool can then grab the lower chip an place it accurately on the chuck. Most processes developed for this machine (including this one) require the user to directly place the lower chip on the chuck. Accurately placing the lower chip is superfluous since the alignment process can correct these inaccuracies. A liquid injector is mounted behind the vacuum tool and can be used to place various fluids on the lower chip. However, due to the excessive maintenance required to use it, we opted to construct our system for glue application, see appendix G.

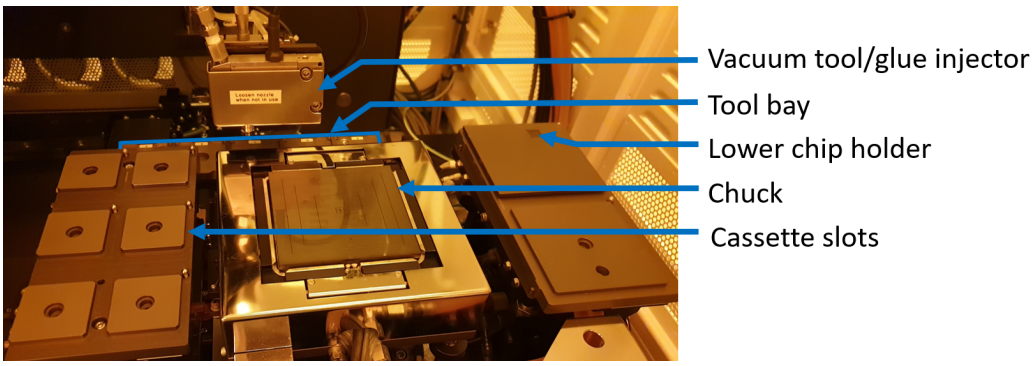

Figure 2.13: Detailed picture of the bottom part of the FC150 chip bonder. The cassette is clamped on a cassette slot array. The arm can grab different tools located on the tool bay before picking up the chip located on the cassette. For the calibration test, a lower chip can be placed on a holder and is transferred on the chuck by the means of a vacuum tool. A glue injector is also mounted on the vacuum tool.

2.3.3 Custom parts for the FC150

For our process, we chose to place the qubit chip on the chuck. This means that the arm's tool will pick up an HBAR chip. The FC150 comes with a default chuck vacuum tool having several vacuum squares allowing it to grab chips ranging from 8mm to 4 inches, see fig.2.14. Unfortunately, even the 8mm square isn't completely covered by the qubit chip which is 3mm by 7mm in size. An adapter mounted on the top of the default chuck tool is used to mitigate this issue. It is a square-shaped, 0.5 mm thick sheet of aluminum with 50 mm side with a 0.8 mm diameter pinhole in the center. The shape of the adapter perfectly matches a pattern on the underlying tool. Once placed correctly, the pinhole is located a the intersection of the vacuum lines in the middle of the 8mm square, see fig.2.15. Any chip able to cover this pinhole will be hold in place by the chuck's vacuum chain.

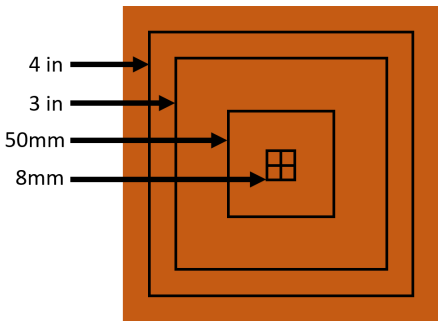

Figure 2.14: The default chuck vacuum tool presents several square vacuum patterns.

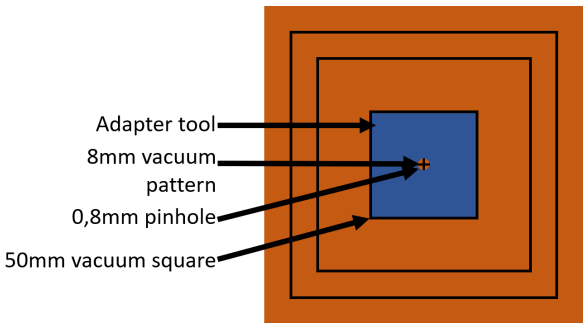

Figure 2.15: Chuck tool with the adapter on can grab any chip who can cover a 0.8 diameter circle.

The arm's default vacuum tool consists of a 1 cm vacuum grid pattern which is larger than the HBAR chip. A new tool was designed with a 5 mm square raised surface in its center. On this surface, a thin slot of 1.5 mm is machined. It is connected to the vacuum system by a hole passing through the tool. Fig.2.16 shows the default and custom tool. Fig.2.17 shows the mechanism allowing the arm to grab the arm's tool. An off-centered pipe grabs the tool while a central vacuum pipe goes thought the tool to grab the upper chip. If the surfaces aren't flat enough*, the vacuum chain is broken and the grabbing fails.

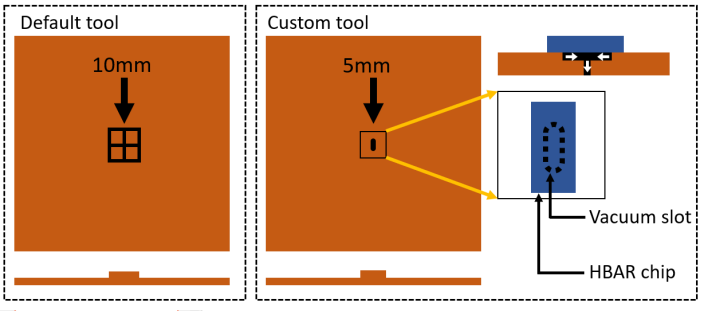

Figure 2.16: Arm's default vacuum tool isn't suited for the dimensions of the HBAR chip. A new tool is designed to grab the HBAR chip with a 1.5 mm vacuum slot. A magnified view of the slots shows how the HBAR fits the slot and a side cut shows how the vacuum chain is closed once the chip is grabbed.

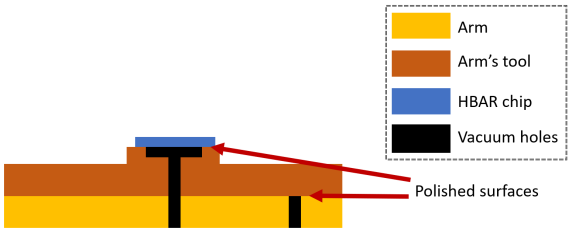

Figure 2.17: The arm is equipped with two kinds of vacuum holes, the first one grabs the tool while the second one passes through the tool to pick the chip (HBAR chip in our case).

The cassette was designed to protect the microlens located on the surface of the chip. On the first depth level, the chip spacers are touching the cassette. On a second depth level, a slot is machined

*the surface profile shouldn't fluctuate more than tens of nanometers per millimeter

beneath the location of the lens. To test the FCB, we are performing preliminary bondings with unused sapphire chips. They are cheaper than the AlN covered sapphire chips used for the HBAR chips[†]. To manipulate them, additional slots are included in the cassette, see fig.2.18. An important criterion for cassette designing is that the upper face of the chip placed on the cassette should rise above the cassette's surface, see fig.2.19.

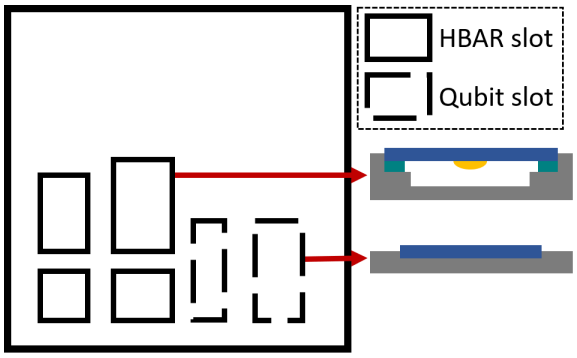

Figure 2.18: The cassette has HBAR slots protecting the micro lens by having an empty space under it. For preliminary tests, one also use basic slots where practise chips can be placed

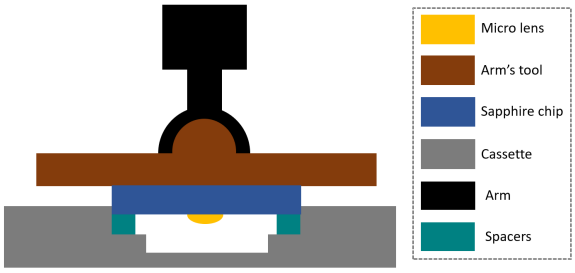

Figure 2.19: For the grabbing procedure to be successful, the depth of the first surface should be smaller than the height of the sapphire chip.

Fig. 2.20 shows the adapter parts introduced in the section for the new bonding process.

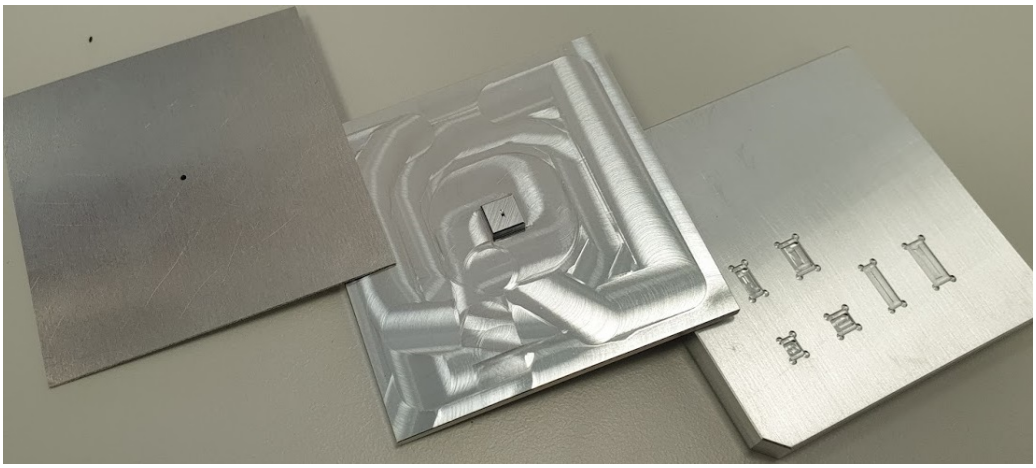

Figure 2.20: Adapter parts used on the FC150, from left to right, the chuck adapter, the arm's tool and the upper chip cassette.

2.3.4 FC150 calibration

The FC150 grants a micrometric alignment precision to the operator if its calibration is performed correctly. The first step is dedicated to the parallelism of the chuck and the arm. The arm's holder is mounted on a z-axis translation stage through a vacuum sphere (behaving as an adjustable spherical joint) thus allowing the tuning of the θ_x and θ_y angles, see fig.2.21. As illustrated in fig.2.21, a mirror is placed on the chuck and a light cross illuminates it. The operator marks the reflection of the cross with a numerical marker on the screen. After transferring the mirror to the arm, the reflected light cross is not matching the numerical marker. The operator corrects this by rotating the sphere and once the cross and marker are matched, the parallelism calibration is done.

[†]coating a sapphire substrate with aluminum nitride is an expensive process

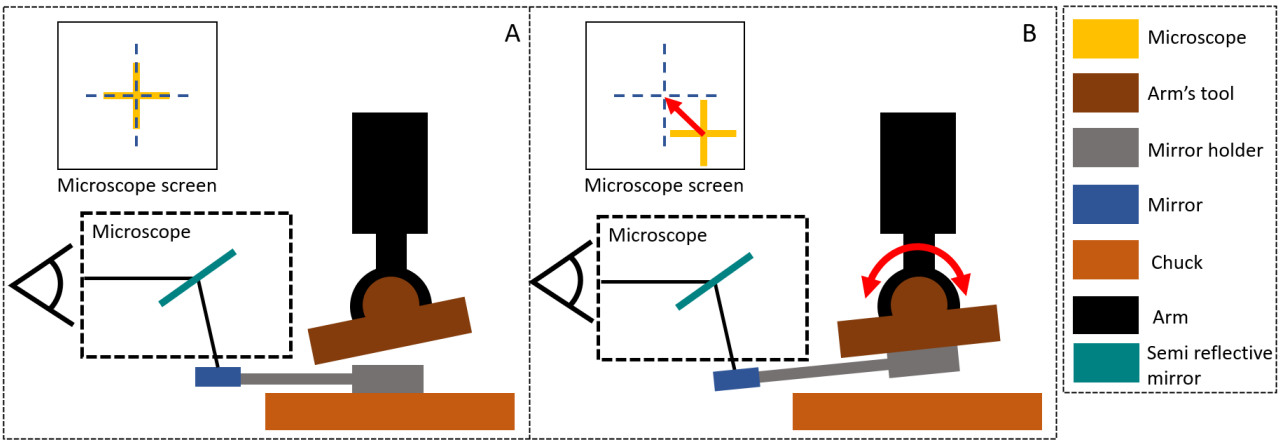

Figure 2.21: The first calibration step ensures parallelism between the arm and the chuck. A: A light cross is projected onto a mirror placed on the chuck. The location of the light cross is marked on the microscope screen (dashed cross). B: After the transfer of the mirror on the arm's tool, the user corrects the parallelism by rotating the arm's holder to match the light cross with the marker.

The parallelism of the two incident optical paths (the one coming from the chuck and the arm) is the next step. Fig. (2.22) illustrates the procedure. A chip is used to reflect a light cross. After marking its location on the screen the chip is transferred to the arm. The light cross is matched with its previous location by the mean of an optical path adjuster. After this step the incident optical paths are parallel.

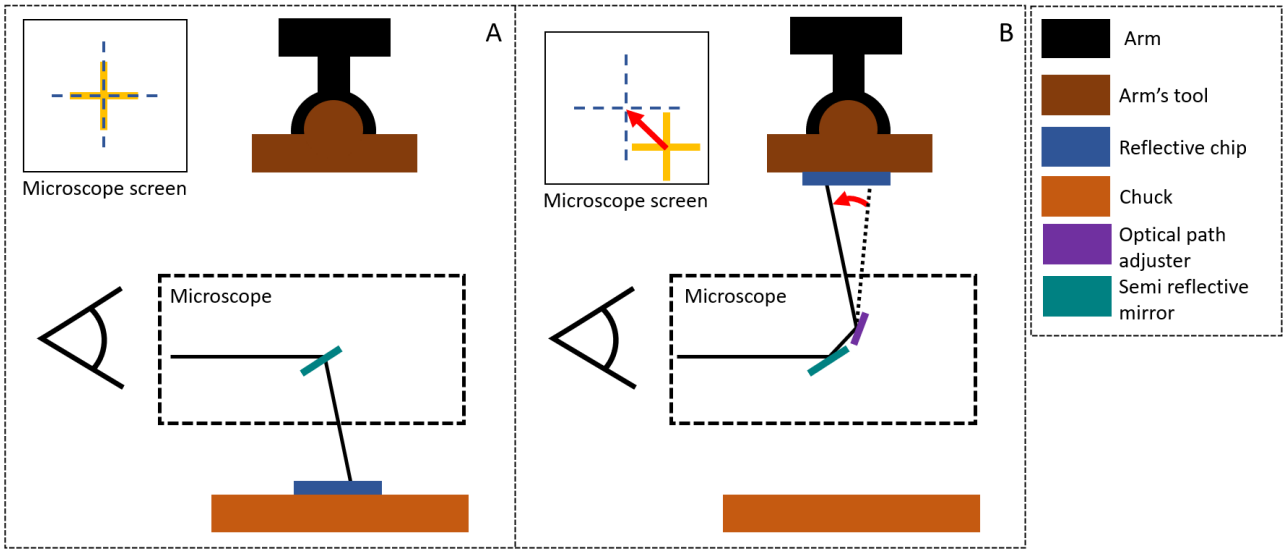

Figure 2.22: The second calibration steps ensure parallelism between the two optical paths. A: A reflective chip is placed on the chuck and the location of the light cross reflection is marked with a crosshair (dashed cross). B: The reflective chip is placed on the arm. The operator matches the reflection of the light cross with the crosshair by using an optical path adjuster. At the end of the process, the two incident paths are parallel

The last step ensures that the two optical paths are looking at the same spots on the two chips. Notice that this setup made of two optical paths is not sensitive to the orthogonality of the beam on the substrate*. For this final task, a chip with an alignment pattern is picked up by the arm and marked on the screen. It is then transferred to the chuck and the two beams are moved in a parallel fashion to match the light cross with the crosshair, see fig.2.23.

*As opposed to a setup where a single optical path is used to go through both chips.

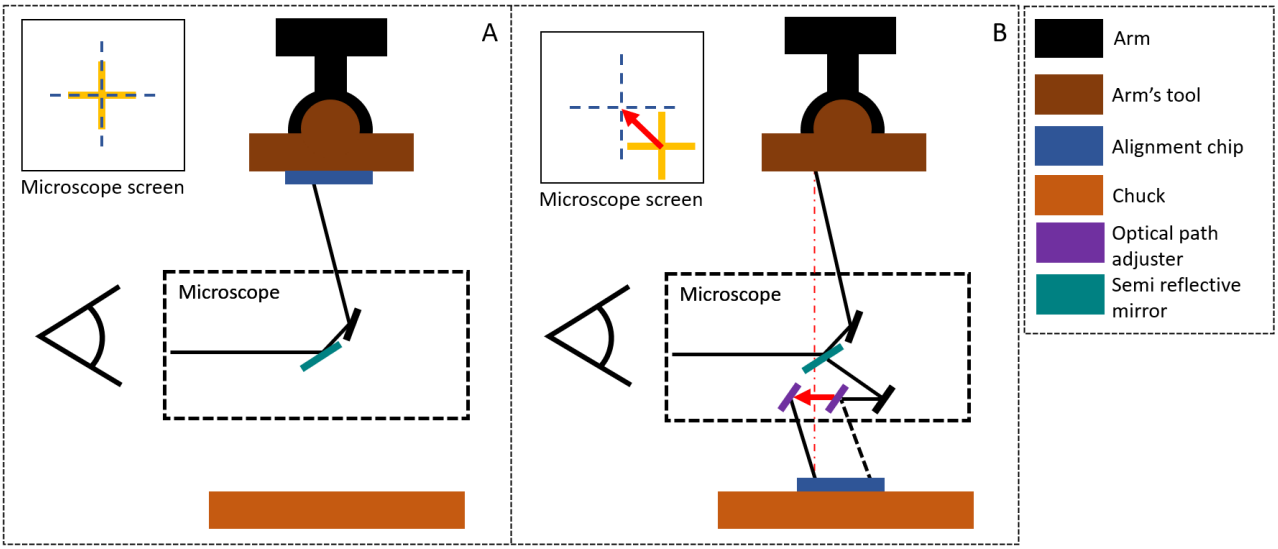

Figure 2.23: The third step ensures the two incident paths are looking at the same points on the two chips. A: A chip with an alignment mark is placed on the arm, the location of the alignment pattern (yellow cross) is marked with a crosshair (dashed cross). B: After transferring the chip on the chuck, the optical path is moved in a parallel manner to match the pattern with the crosshair.

2.3.5 FC150 bonding cycle

In this section, we describe how we use the FC150 chip bonder to bond an HBAR chip to a qubit chip. The chip bonder is calibrated, see section 2.3.4 and equipped with the adapter tools, see section 2.3.3. To ensure that the parallelism between the chuck and arm surfaces is preserved after we have equipped the adapter parts, a procedure known as autocollimation is performed. The HBAR chip is grabbed by the arm's tool. A qubit chip that already has bonding agent drops on its surface is placed on the chuck. The chips are then aligned by the operator through a step called θ_z correction (described in detail in appendix B). The chips are placed in close contact until the HBAR chip spacers are touching the qubit chip. Finally, a heat cure is applied to the chips to harden the bonding agent drops. A detailed description of the bonding protocol is presented in appendix C.

2.3.6 Bonding agent selection and deposition method

In this section, we motivate the choice of bonding agent by reviewing the constraints imposed by the flip-chip geometry and the use of the FC150 chip bonder. To conclude this part, we present a deposition technique enabling accurate placement of the bonding agent on the chips.

Using the FC150 chip bonder imposes a latency of several minutes between the moment we place the chips in the machine and the final bonding. The bonding agent needs to preserve its adhesiveness for several minutes. The glue that was used in the previous FCB is thus no longer suited. Therefore, we need to find a glue whose curing is activated by a controllable physical process. For instance, a heat cure epoxy* could be placed ahead of the bonding and cured by eating the chuck and the arm at 120°C. Note that we cannot go beyond this temperature without risking to break the qubit's Josephson junctions. Another approach would be to use an UV glue called NOA61† curable in less than 10 seconds with a special UV light torch‡.

As fig.2.7 illustrates, the bonding agent needs to be placed accurately and in small quantities. The use of a picoliter injector in the cleanroom was first considered. As shown in fig.2.24, this kind of device is compact but requires an input of compressed air which does not ease its integration in the

*https://www.permabond.com/2015/11/24/heat-cure-epoxy-making-adhesive-properly-cured/
†https://www.norlandprod.com/adhesives/NOA%2061.html
‡http://www.techoptics.com/media/2200/opticure-led-200.pdf

laboratory. Two other drawbacks were identified. Firstly, for each drop of bonding agent that we want to place on the chip, we have to align the needle of the injector with the help of a microscope. Secondly, the glues we want to use may have a too high viscosity for the injector to work properly.

A process known as *microcontact printing technique* [33] was finally implemented. We fabricate a stamp of silicon polymers to transfer photoresist drops on the qubit chip. The recipe for the stamp is given in the appendix E while the description of the alignment setup built to move accurately the stamp between the silicon wafer and the qubit chip is described in appendix G. The shape of the stamp is sketched on fig.2.25. It is designed to place drops of bonding agent on the qubit chip such that after the bonding these drops will touch the corners of the HBAR chip. It is possible to add more cylindrical features to reinforce the bonding or change the width of the cylindrical features to lower the size of the bonding agent drops. The transfer process using it is described in fig.2.26.

Figure 2.24: Commercial pico-liter injector

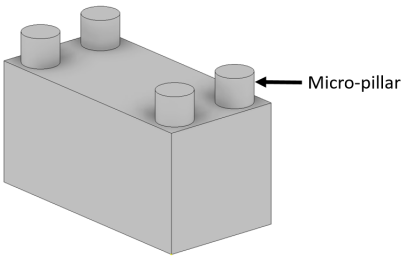

Figure 2.25: The stamp has the shape of a rectangular box with 4 cylinders (also called micro-pillars) on one surface. These cylinders have a height of 120 µm. Image scale is not respected.

The photoresist compatible with this transfer process that we use for all the bonding is *SU-8 GM1050*[*] produced by Gersteltec. It is a negative photoresist presenting good mechanical strength once it has been cross-linked. In our process, we cross-link the photoresist by heating the chuck and the arm of the FC150 chip bonder at 120°C for 5 minutes. We chose to use this type of photoresist because it takes several minutes before it dries out. This means that the operator can repeat the transfer process shown on fig.2.26 up to 3 times. To perform more transfers, we need to clean the silicon wafer and spin-coat a new photoresist layer. The solvent used in SU-8 GM1050 is *GBL* (gamma-butyrolactone). It shows great compatibility with the transfer process, meaning that it sticks to the stamp and also to the qubit chip made of sapphire. We also tried another SU-8 called *SU-8 3005*[†] produced by MicroChem. The solvent used for this photoresist is *PGMEA* (Propylene glycol methyl ether acetate). The latter is not compatible with our process since it does not stick to the stamp.

We were also interested in the idea of having a reversible bonding. We could then imagine a protocol in which we bond temporarily the HBAR chip to a resonator chip. The latter is much simpler to fabricate than a qubit chip and is designed to test the quality of the HBAR. After having selected the best HBAR chips, we could proceed by bonding them on qubit chips. SU-8 is hard to dissolve once it has been cross-linked. Furthermore, we cannot use any strong acid since this would also dissolve the piezoelectric material feature on the HBAR chip. We tried a positive photoresist called *AZ MIR 701*[‡] which is dissolvable in an organic solvent. The solvent used for this photoresist is *novolak*. The latter was sticking to the stamp but dried out before we had the time to apply the stamp on the sapphire chip. A suitable bonding agent will still have to be found in the future for reversible bonding.

[*] https://www.gersteltec.ch/wp-content/uploads/2019/05/GM1050_v1.0.pdf
[†] https://engineering.dartmouth.edu/microeng/processing/lithography/SU83000DataSheet.pdf
[‡] https://www.microchemicals.com/products/photoresists/az_mir_701.html

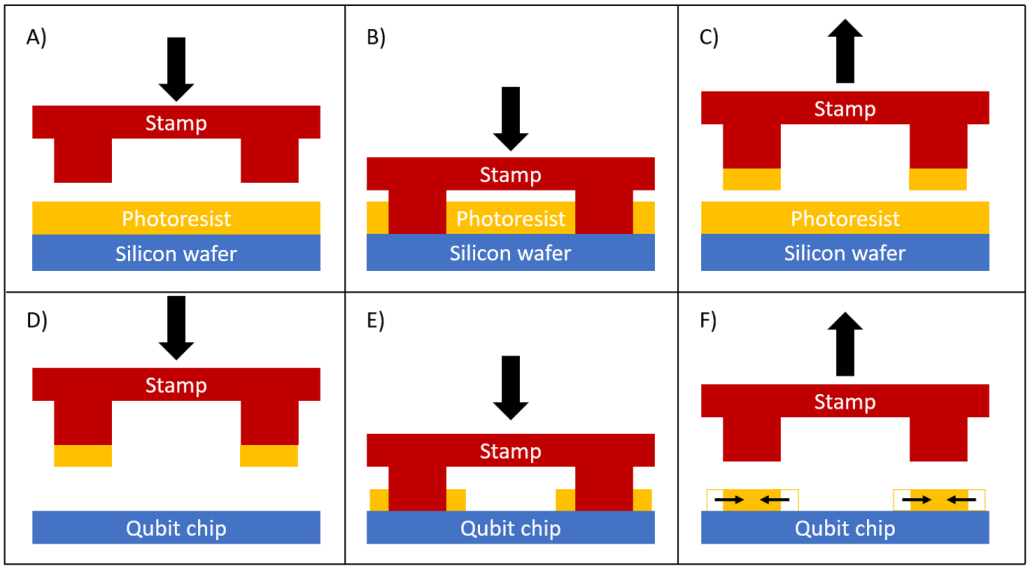

Figure 2.26: Side cut of the photoresist transfer process. A: A photoresist is spin-coated on a silicon wafer, a stamp with cylindrical features is approached on the surface. B: The operator lowers the stamp until it touches the silicon wafer, for a clean transfer process, the upper part of the stamp shouldn't touch the photoresist. C: When the separation is increased, the PDMS cylinder tops grab the photoresist. D: The operator aligns the stamp with an alignment setup described in appendixG on the qubit chip to accurately select the locations where the glue drops will be deposited. E: The separation is lowered until the stamps contacts the chip, at this point, the photoresist spreads around the cylinders in a ring-like shape. F: The operator removes the stamp and due to capillarity, the photoresist rings evolve into dome-like shapes.

We tested different stamps having cylindrical features of various diameters. The best results were obtained with cylindrical features of 300 µm of diameter. The shape of the drops was analyzed by using a confocal microscope, see fig.2.27. We can see that the final diameter of the drop is less than a third of the initial one given by the feature's diameter. This shows the effect of surface tension on the SU-8 drop. This is crucial to produce a drop thick enough in its bulk so that it can make contact between the two chips. The maximal height is about 8.8μm which ensures good contact between the two chips having 5 µm spacers.

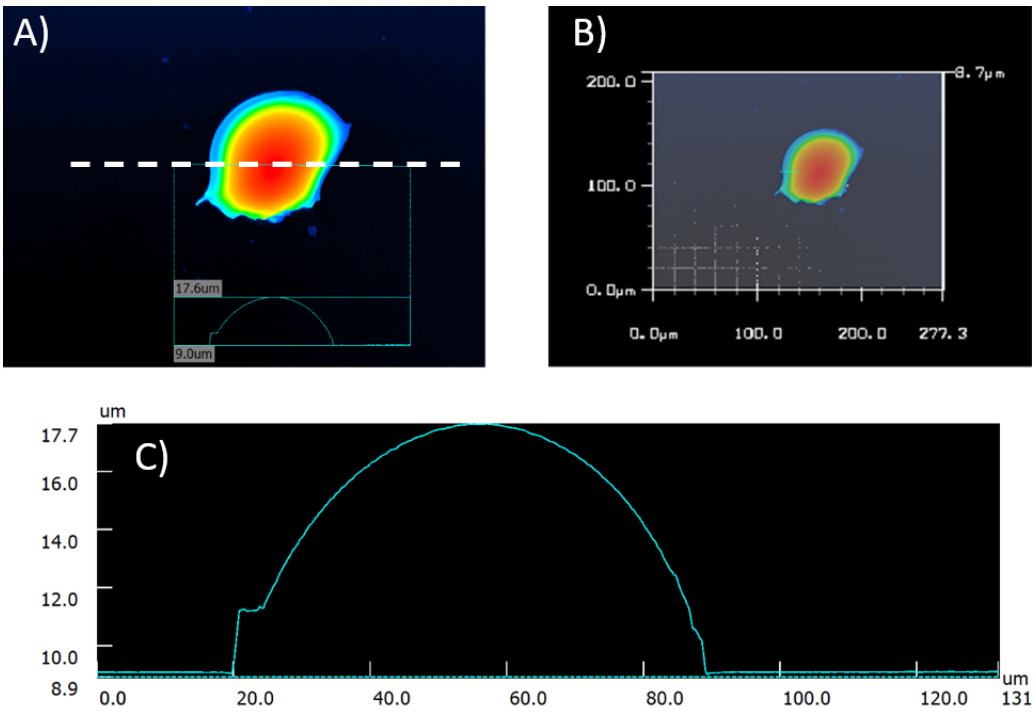

Figure 2.27: Confocal microscope observation of a SU-8 drop made with cylindrical features of 300 µm of diameter. A) Color map of the drop, the dashed white line represents the cut section shown in C). B) The spreading of the drop is smaller than 100μm. C) Height scan of the drop shows a maximal height of $17.7 - 8.9 = 8.8\mu$m

Chapter 3

Results and conclusion

3.1 Results

In this section, we present the results from the bonding procedure which has been performed 8 times. Fig.3.1 gives some visuals of the assembled hybrid quantum system.

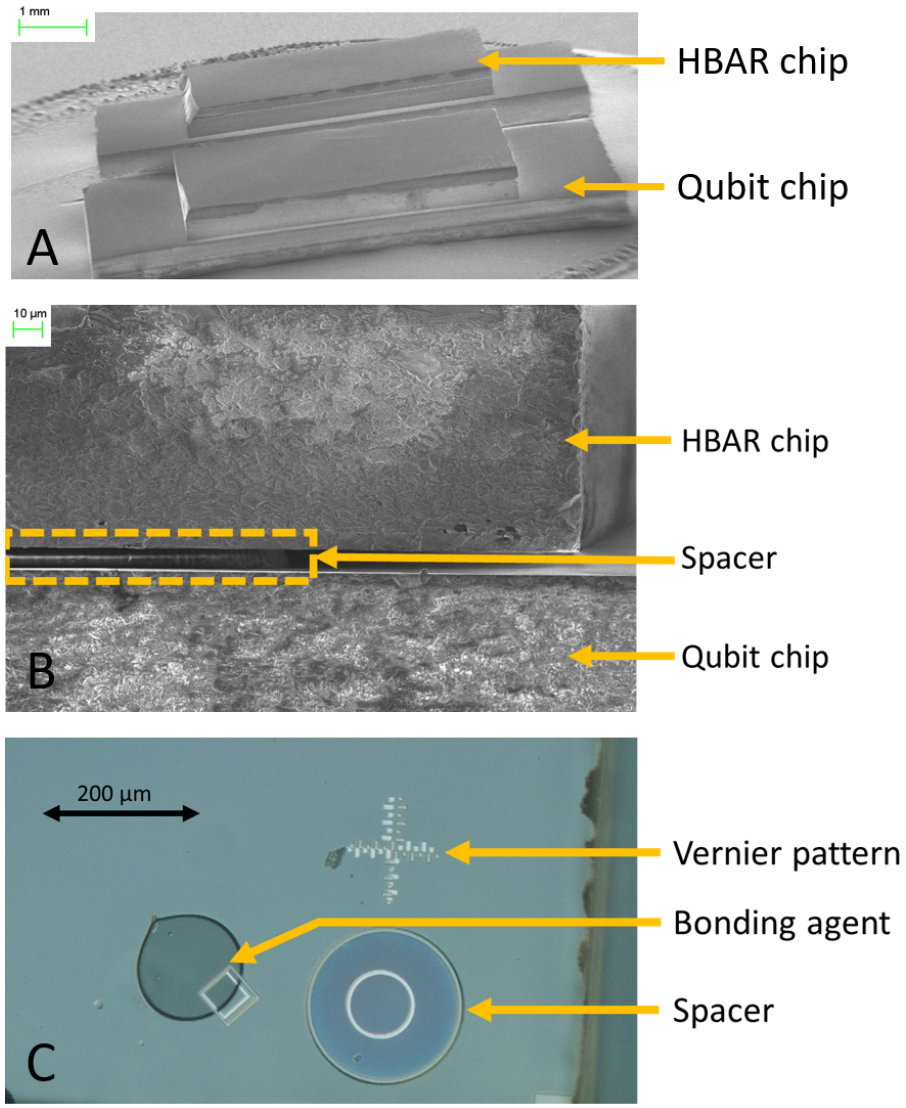

Figure 3.1: A: SEM picture showing two flip-chip devices. B: SEM picture showing a close-up view of the inter-chip, the separation on this side is about 5.7 µm. C: Optical microscope picture showing a top view of the bonded HBAR chip's corner. The Vernier patterns are mismatched by 6 µm. The drop of bonding agent has a width of 120 µm which corresponds to a SU-8 volume of 68 pL.

The alignment marks can be matched up to 6 µm. It is believed that better accuracy is reachable for a more experienced user. The tilting angle θ_x* was estimated by measuring the inter-chip distance from two opposite sides. On average, we obtained $\theta_x \approx 0.01°$. In terms of distance, this translates into a relative change of spacing of 360 nm. Increasing the amount of force applied on the chips by the chip bonder arm may lower this value. For all these tests, the baking recipe was set to 5 minutes at 120°C, and 4 drops each containing approximately 70 pL of SU-8 were placed between the corners of the HBAR chip and the qubit chip. It should be mentioned that the alignment accuracy between the qubit's antenna and the HBAR's microlens is not directly linked to the matching of the alignment marks. The fabrication of the alignment marks relies on two mask aligning operations. If we assume that the mask alignment is accurate up to 3 µm, then in the worst case, all these inaccuracies could sum up. This gives an upper bound for the misalignment, $\Delta\mu < 13$ µm which is still under the bound we derived in section 1.3.

When the operator has to bond many chips, it is possible to parallelize the protocol to increase the time efficiency in the cleanroom. Once the silicon wafer is coated with SU-8, the operator should transfer the SU-8 drops on 3 chips. The time needed for this is roughly matching the time that the SU-8 takes to dries out on the wafer. Then the operator can start bonding the chips in the FC150 chip bonder. When the bonder bakes the chips, the operator can start cleaning the silicon wafer and spin-coat a new layer of SU-8. This protocol gives an average time per bonding of 15 minutes.

3.2 Conclusion

We were able to bond two quantum devices with a precision that meets the requirements derived in the introductory section. This was made possible through the use of an industrial chip bonder which was customized to the dimensions of our chips. SU-8 GM1050 was chosen to be the bonding agent as it is compatible with the stamp transfer technique we developed. To accurately place the bonding agent on the chip we built an alignment setup. This one offers great versatility and can be easily modified in the future if the shapes of the chips or the stamps evolve. Further investigations are still required to find another kind of bonding agent dissolvable in an organic solvent. The SU-8 GM1050 is cured in the chip bonder. Other curing recipes could be tested to make sure that the SU-8 is fully cross-linked. For instance, adding a UV exposure session after the thermal curing process. More bonding trials could be performed to see if the quantity of bonding agent can be reduced without impacting on the bond solidity. Implementing a glue transfer process using the chip bonder could increase the time efficiency of the whole bonding process as well as its reproducibility. The first step towards that direction was made by creating slots on the cassette where the soaked stamps can be placed.

*rotation along the longest side of the HBAR chip

Bibliography

[1] R. P. Feynman, "Simulating physics with computers," *Int. J. Theor. Phys*, vol. 21, no. 6/7, 1999.

[2] S. Lloyd, "Universal quantum simulators," *Science*, vol. 273, no. 5278, pp. 1073–1078, 1996. [Online]. Available: http://www.jstor.org/stable/2899535

[3] R. Barends, L. Lamata, J. Kelly, L. García-Álvarez, A. Fowler, A. Megrant, E. Jeffrey, T. White, D. Sank, J. Mutus *et al.*, "Digital quantum simulation of fermionic models with a superconducting circuit," *Nature communications*, vol. 6, no. 1, pp. 1–7, 2015.

[4] J. Aasi, J. Abadie, B. Abbott, R. Abbott, T. Abbott, M. Abernathy, C. Adams, T. Adams, P. Addesso, R. Adhikari *et al.*, "Enhanced sensitivity of the ligo gravitational wave detector by using squeezed states of light," *Nature Photonics*, vol. 7, no. 8, p. 613, 2013.

[5] X.-B. Chen, T.-Y. Wang, J.-Z. Du, Q.-Y. Wen, and F.-C. Zhu, "Controlled quantum secure direct communication with quantum encryption," *International Journal of Quantum Information*, vol. 6, no. 03, pp. 543–551, 2008.

[6] M. H. Devoret, A. Wallraff, and J. M. Martinis, "Superconducting qubits: A short review," *arXiv preprint cond-mat/0411174*, 2004.

[7] H. Häffner, C. F. Roos, and R. Blatt, "Quantum computing with trapped ions," *Physics reports*, vol. 469, no. 4, pp. 155–203, 2008.

[8] G. Wu and N.-Y. Lue, "Graphene-based qubits in quantum communications," *Physical Review B*, vol. 86, no. 4, p. 045456, 2012.

[9] F. Arute, K. Arya, R. Babbush, D. Bacon, J. C. Bardin, R. Barends, R. Biswas, S. Boixo, F. G. Brandao, D. A. Buell *et al.*, "Quantum supremacy using a programmable superconducting processor," *Nature*, vol. 574, no. 7779, pp. 505–510, 2019.

[10] M. Kjaergaard, M. E. Schwartz, J. Braumüller, P. Krantz, J. I.-J. Wang, S. Gustavsson, and W. D. Oliver, "Superconducting qubits: Current state of play," *Annual Review of Condensed Matter Physics*, vol. 11, 2019.

[11] A. G. Fowler, M. Mariantoni, J. M. Martinis, and A. N. Cleland, "Surface codes: Towards practical large-scale quantum computation," *Physical Review A*, vol. 86, no. 3, p. 032324, 2012.

[12] Z.-L. Xiang, S. Ashhab, J. You, and F. Nori, "Hybrid quantum circuits: Superconducting circuits interacting with other quantum systems," *Reviews of Modern Physics*, vol. 85, no. 2, p. 623, 2013.

[13] X. Han, C.-L. Zou, and H. X. Tang, "Multimode strong coupling in superconducting cavity piezoelectromechanics," *Physical review letters*, vol. 117, no. 12, p. 123603, 2016.

[14] M. J. Schütz, "Universal quantum transducers based on surface acoustic waves," in *Quantum Dots for Quantum Information Processing: Controlling and Exploiting the Quantum Dot Environment*. Springer, 2017, pp. 143–196.

[15] Y. Chu, P. Kharel, W. H. Renninger, L. D. Burkhart, L. Frunzio, P. T. Rakich, and R. J. Schoelkopf, "Quantum acoustics with superconducting qubits," *Science*, vol. 358, no. 6360, pp. 199–202, 2017.

[16] R. Manenti, A. F. Kockum, A. Patterson, T. Behrle, J. Rahamim, G. Tancredi, F. Nori, and P. J. Leek, "Circuit quantum acoustodynamics with surface acoustic waves," *Nature communications*, vol. 8, no. 1, pp. 1–6, 2017.

[17] Y. Chu, P. Kharel, T. Yoon, L. Frunzio, P. T. Rakich, and R. J. Schoelkopf, "Creation and control of multi-phonon fock states in a bulk acoustic-wave resonator," vol. 563, no. 7733. Nature Publishing Group, 2018, p. 666.

[18] A. Perl, D. N. Reinhoudt, and J. Huskens, "Microcontact printing: limitations and achievements," *Advanced Materials*, vol. 21, no. 22, pp. 2257–2268, 2009.

[19] V. Bouchiat, D. Vion, P. Joyez, D. Esteve, and M. Devoret, "Quantum coherence with a single cooper pair," *Physica Scripta*, vol. 1998, no. T76, p. 165, 1998.

[20] B. Joesphson, "Possible new effects in superconductive tunneling," *Phys. Lett*, vol. 1, no. 7, p. 251, 1962.

[21] L. N. Cooper, "Bound electron pairs in a degenerate fermi gas," *Phys. Rev.*, vol. 104, pp. 1189–1190, Nov 1956. [Online]. Available: https://link.aps.org/doi/10.1103/PhysRev.104.1189

[22] C. Kachhava, *Solid State Physics, Solid State Device And Electronics.* New Age International, 2003.

[23] J. Koch, T. M. Yu, J. Gambetta, A. A. Houck, D. I. Schuster, J. Majer, A. Blais, M. H. Devoret, S. M. Girvin, and R. J. Schoelkopf, "Charge-insensitive qubit design derived from the cooper pair box," *Phys. Rev. A*, vol. 76, p. 042319, Oct 2007. [Online]. Available: https://link.aps.org/doi/10.1103/PhysRevA.76.042319

[24] C. D. Tesche, "Analysis of a double-loop dc squid," *Journal of Low Temperature Physics*, vol. 47, no. 5-6, pp. 385–410, 1982.

[25] T. Brecht, M. Reagor, Y. Chu, W. Pfaff, C. Wang, L. Frunzio, M. H. Devoret, and R. J. Schoelkopf, "Demonstration of superconducting micromachined cavities," *Applied Physics Letters*, vol. 107, no. 19, p. 192603, 2015.

[26] R. Manenti, A. F. Kockum, A. Patterson, T. Behrle, J. Rahamim, G. Tancredi, F. Nori, and P. J. Leek, "Circuit quantum acoustodynamics with surface acoustic waves," *Nature communications*, vol. 8, no. 1, p. 975, 2017.

[27] A. Clerk, K. Lehnert, P. Bertet, J. Petta, and Y. Nakamura, "Hybrid quantum systems with circuit quantum electrodynamics," *Nature Physics*, pp. 1–11, 2020.

[28] K. J. Satzinger, Y. Zhong, H.-S. Chang, G. A. Peairs, A. Bienfait, M.-H. Chou, A. Cleland, C. R. Conner, É. Dumur, J. Grebel *et al.*, "Quantum control of surface acoustic-wave phonons," *Nature*, vol. 563, no. 7733, pp. 661–665, 2018.

[29] W. Renninger, P. Kharel, R. Behunin, and P. Rakich, "Bulk crystalline optomechanics," *Nature Physics*, vol. 14, no. 6, pp. 601–607, 2018.

[30] K. T. McDonald, "Conducting ellipsoid and circular disk," 2019. [Online]. Available: http://puhep1.princeton.edu/~kirkmcd/examples/ellipsoid.pdf

[31] A. Chow, D. Hopkins, R. Ho, and R. Drost, "Measuring 6d chip alignment in multi-chip packages," pp. 1307–1310, Oct 2007.

[32] D. J. Pedder, "Vernier structure for flip chip bonded devices," Jun. 11 1991, uS Patent 5,022,580.

[33] J. L. Wilbur, A. Kumar, H. A. Biebuyck, E. Kim, and G. M. Whitesides, "Microcontact printing of self-assembled monolayers: applications in microfabrication," *Nanotechnology*, vol. 7, no. 4, p. 452, 1996.

Appendices

Appendix A

SU-8 spacer recipe

The spacers are made of SU-8 3005, a negative photoresist presenting good mechanical strength once it has been cross-linked.

1. Coat the sapphire wafer with HMDS for 10 minutes (without this step the layer of spin coated photoresist will bead on the substrate).
2. Place the wafer in the spin-coater and pour SU-8 3005 (SU-8 3005 is an improved version of SU-8 2005, it sticks better to surfaces and is less sensitive to temperature ramping for the soft bake). Perform the following spinning recipe.
3.

spinning recipe	
seconds	rpm
6	6000
30	6000
6	0

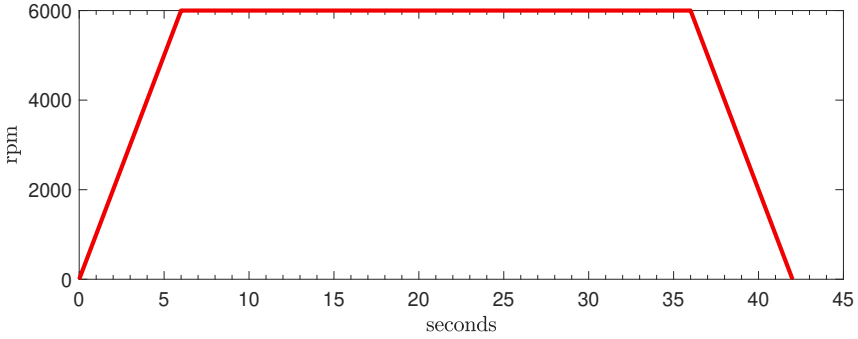

4. Let the substrate rest for 5 minutes.
5. Soft bake the wafer at 95°C for 180 seconds on a hotplate.
6. Expose with a dose of 187.5 mJ/cm^2 at a wavelength of 365nm.
7. Perform the post-exposure bake by preparing two hot plates, one at 65°C and another at 95°C. Bake the substrate for 60 seconds on the former and 120 seconds on the latter.
8. Develop for 90 seconds in MR DEV 600.
9. Perform twice the following rinse and develop recipe: place the wafer in IPA for 10 seconds and back in the developer for 10 seconds.
10. Clean with IPA and dry the wafer.

The spacers produced by this recipe were analysed by a profilometer. Fig.A.1 shows the typical profile of spacers located at the middle of the wafer and around its edge. The resting step of five minutes before the soft bake helped to reduce the height different as it is illustrated on fig.A.2. The average height of the spacer's upper portion is 4.23±0.02 µm. The spacer heights difference fluctuates by less than a hundred micrometer over a scanning distance covering the upper part of the spacer which serves to set the inter-chip spacing.

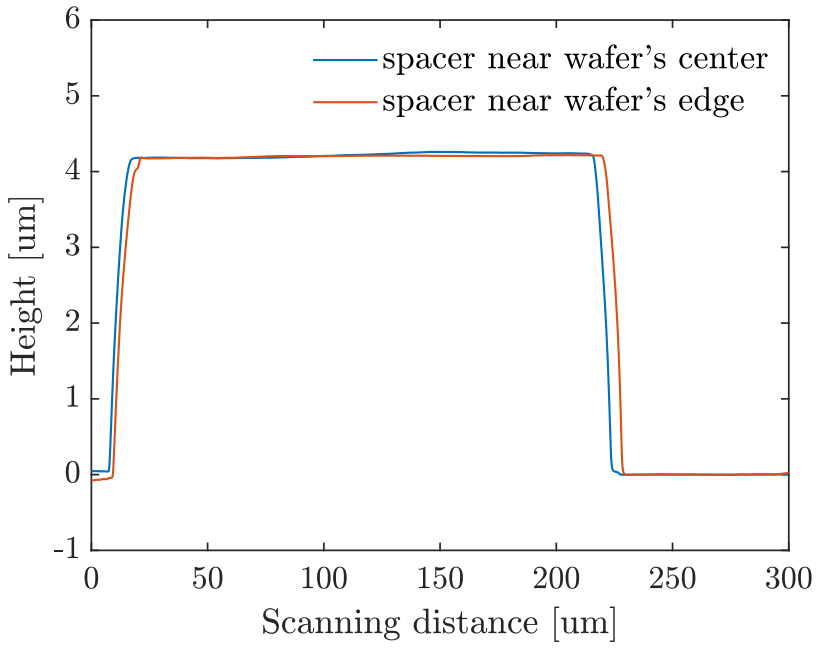

Figure A.1: Profile comparison of SU-8 spacers placed in the middle and at the edge of the wafer. The averaged height for these spacers is 4.23±0.02 µm.

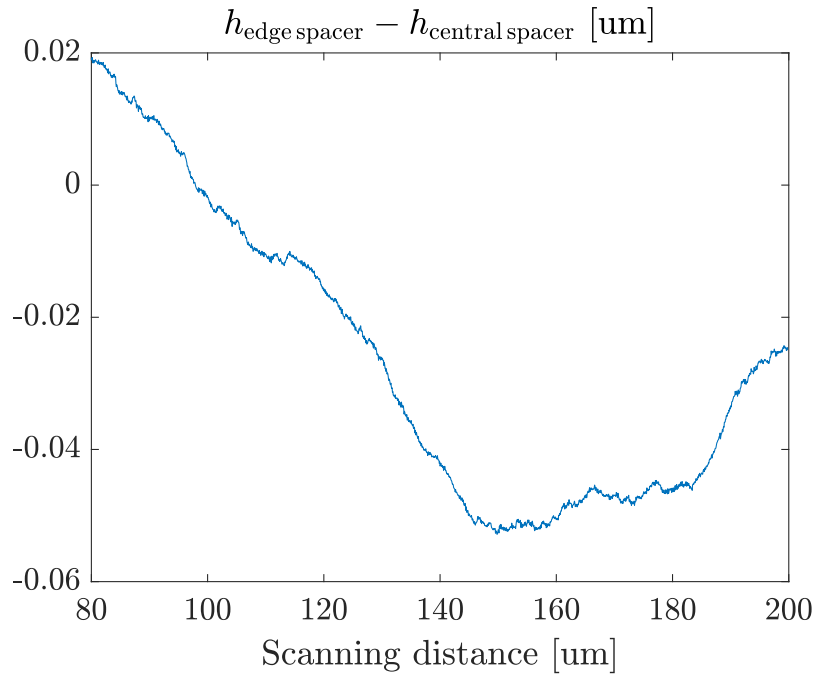

Figure A.2: Difference of the profiles reported on fig.A.1. We only show the difference from 80 µm to 200 µm for a better visibility and also because only the upper faces of the spacers is used to set the inter-chip spacing.

Appendix B

SET FC150, automatic θ_z correction

When the operator starts the theta correction procedure in the alignment function of the FC150, only translations along the x and y axis need to be corrected manually. Rotational misalignment along the z axis is computed automatically by the FC150. Fig. B.1 explains the principle of the alignment routine.

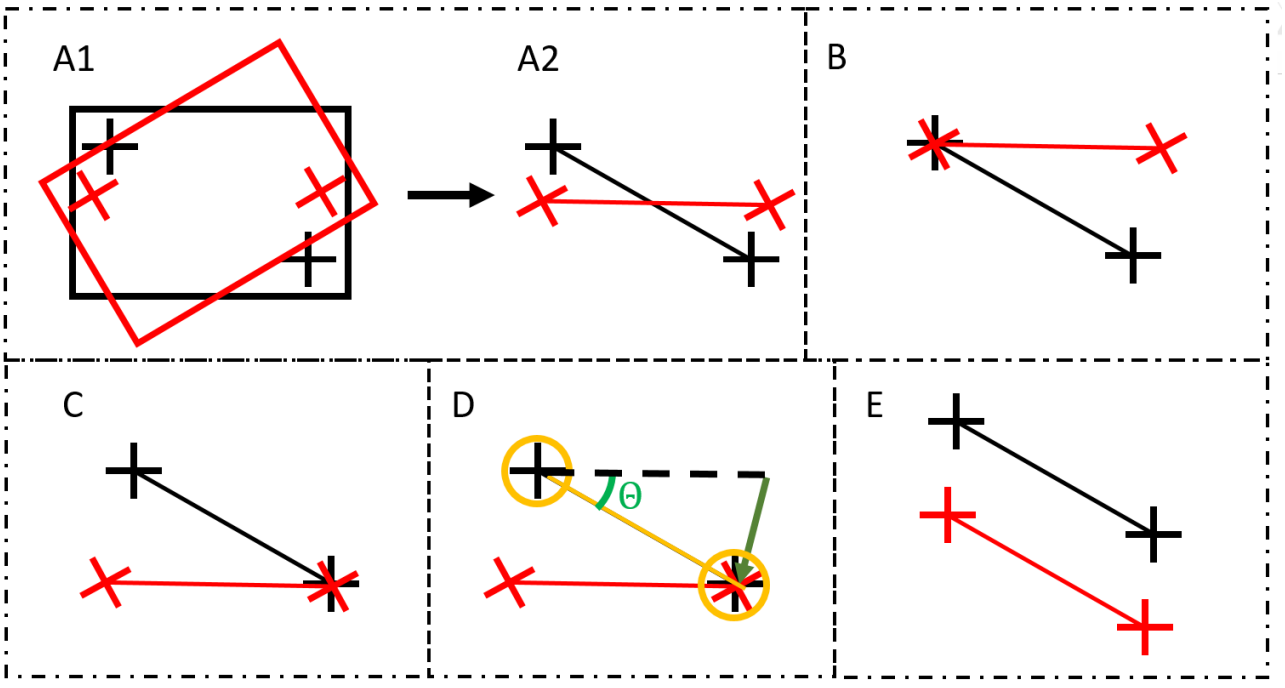

Figure B.1: This series of sketch describes an ideal iteration of the θ_z correction routine. In reality, because the operator never matches perfectly the marks, the alignment should be performed several times. A1: The chip is represented by rectangles, the crosses represent the alignment marks. Red indicates the upper chip and black the lower chip. Recall that the arm cannot move nor rotate so all the alignment corrections are performed on the bottom chip. A2: We simplify the appearance of the chips to ease the illustration. B: The operator matches the first couple of marks. The position of the microscope is saved before the operator moves to a second couple of marks. C: The operator matches a second couple of alignment marks. When this is done, he indicates it to the machine who saves the location of the microscope. D: The machine has in memory the two microscope locations used for the alignment (yellow circle). The effective misalignment angle θ_z is computed. E: The chuck automatically rotates and in this ideal case, the chips are aligned if the operator corrects the misalignment along the x and y axis.

Appendix C

FC150 bonding protocol

We describe the required steps that should be executed with the FC150 chips bonder to bond an HBAR and qubit chips together.

1. Perform the calibration described in section 2.3.4.
2. In the *manual mode*, select the function group *load*. Then, use the function *load/unload a substrate manually* and click on *execute* and press *OK*. Press F2 to turn off the vacuum. Place the chuck's custom tool and close the vacuum chain by adding a small rectangular mirror in the center of the tool. Press F2 to turn on the vacuum and make sure the mirror holds in place, press *OK*.
3. Set the cassette definitions. Upper to *AAtUniv1* and lower to *AA_Dummy*. Click on *set cassette*.
4. Set the substrate definition to *adjust* click on *set substrate*.
5. Mount the *universal cassette* on the upper right slot of the 3 by 2 array of cassette slots.
6. Place the custom arm's tool in slot A of the tool bay.
7. Place the smallest rectangular mirror on the *universal cassette* with the reflective face facing down.
8. In the *manual mode*, select the function group *load*. Then, use the function *Chip from Cassette to Arm*, click on *execute*, a window will open, make sure to tick the box corresponding to *align* option. Move the microscope until seeing the microscope's light ray touching the center of the arm's tool. Change the focus parameter for the arm's optical path to 182 000. The vacuum slot of the arm should be visible. Focus the cassette and translate it until seeing the microscope's light ray of light touching the middle of the mirror. Press *OK* and *yes*. The small mirror should now be attached to the arm's tool.
9. In the *manual mode*, select the function group called *chuck position*. Then, use the function *chuck positioning*, click on *execute* and *OK*.
10. In the *manual mode*, select the function group *alignment* and then use the function *alignment*, click on *execute* and *OK*. Then press F7 to start the *autocollimation(chip parallelism)* procedure. Click on *center*. Use the left joystick to rotate the arm and correct the parallelism. After the procedure, the two light crosses should match. Press *OK* and *yes* to exit the chip parallelism mode and press *OK* and *yes* to exit the alignment mode.
11. In the *manual mode*, select the function group *unload*. Then, use the function *Chip from Arm to Cassette*, make sure that the option *tool unload* is not selected.
12. Take the mirror out of the cassette.
13. Mount the *custom cassette* on the upper right slot of the 3 by 2 array of cassette slots.

14. Place an *HBAR* chip in its corresponding cassette slot, make sure that the chip's features are facing down. In the *manual mode*, select the function group *load*. Then, use the function *Chip from Cassette to Arm*, after clicking on *execute*, a window will open, make sure to tick the box corresponding to the *align* option. Focus on the arm's tool and move the microscope until the end of the vacuum slot is at the bottom of the screen, see fig.C.1. Focus the cassette and translate it until seeing the middle of the bottom of the *HBAR* chip, see.C.1. Check that the HBAR faces down by making sure that the spacers and the first depth level of the cassette are simultaneously on focus, you should see a circle corresponding to a SU-8 spacer and micro-scratches corresponding to the surface of the cassette. Press F10 to see both the arm's tool and the cassette. Check that the arm's tool vacuum slot is not extending out of the HBAR. Press *OK* and *yes*. The HBAR should now be attached to the arm's tool.

15. In the *manual mode*, set the substrate definition to *CHU_subs* and click on *set substrate*.

16. In the *manual mode*, select *load*. Then, use the function *load/unload a substrate manually*. click *OK*. Turn the chuck's vacuum off and remove the mirror. Place a *qubit chip* having drops of bonding agent on its surface on the chuck's tool. One of the narrow edges of the chip should be facing the operator, this ensures that the *HBAR* and *qubit* chips are not misaligned by an angle $\theta_z = 90°$.

17. In the *manual mode*, select the function group called *chuck position*. Then, use the function *chuck positioning*, click on *execute* and *OK*.

18. In the *manual mode*, select the function group called *alignment* and then use the function *alignment*, press *OK*. Press F8 to start the *theta correction* procedure. Make sure to focus the alignment marks and not their shadows, the focusing parameter of the arm's optical path should be around 177 000. After the alignment press *OK* and *yes*. The chips are aligned. Details about the automatic theta correction are available in appendix B.

19. In the *manual mode*, select the function group *bonding cycle* and then the function *thermocompression cycle*. Click on *execute* and press *OK*. Start the thermocompression cycle.

20. Once the baking is finished, unload the chips. Proceed with care as the chuck is still hot.

21. To change the baking recipe, go in the *library window* and select the thermocompression cycle associated with the substrate *CHU_subs*. It is called *CHU_thermo*. Open it and edit the baking recipe. Once this is done, *refresh the substrate library* in the *manual mode*, under the *substrate definition* frame. Reassigned the substrate to make sure the new recipe is loaded.

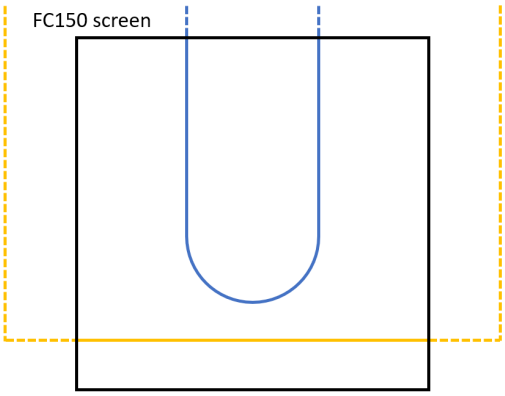

Figure C.1: To grab the HBAR chip (orange contour), the operator has to translate the lower cassette such that the middle of the bottom of the HBAR chip is visible. At the same time, the lower part (relative to the FC150 screen) of the arm tool's vacuum slot (blue contour) should be distant from the edge of chip by $\approx 100\,\mu m$ as presented on the scheme.

Appendix D

Thin layer of SU-8 GM1050

A thin layer of SU-8 GM1050 has to be prepared for the drop deposition process.

1. Use a 4 inches silicon wafer cleaned with acetone and IPA.
2. Bake the wafer on a hotplate at 180 °C to evaporate the water residuals.
3. Place the wafer in the spin-coater and pour SU-8 GM 1050 to cover half of its surface. Perform the following spinning recipe:
4.

spinning recipe	
seconds	rpm
5	500
5	3000
25	3000
5	0

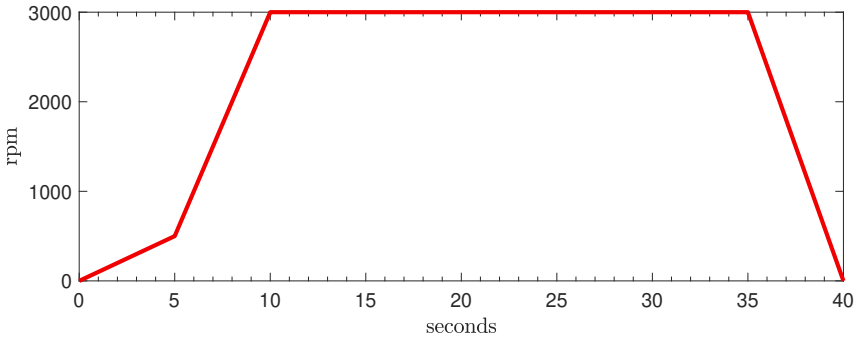

5. Let the substrate rest for 5 minutes to have a homogeneous layer of SU-8.
6. Place the substrate face up in an opaque wafer box to prevent the light from cross-linking the SU-8.

Appendix E

Stamps fabrication

The stamps are made of PDMS, a silicon polymer. When the PDMS mixture is prepared, it is liquid. It has to be poured into a mold and baked for 2 hours to harden. The PDMS is then unmolded and diced. The recipe for the mold is detailed in appendixF. Fig.E.1 illustrate the concept.

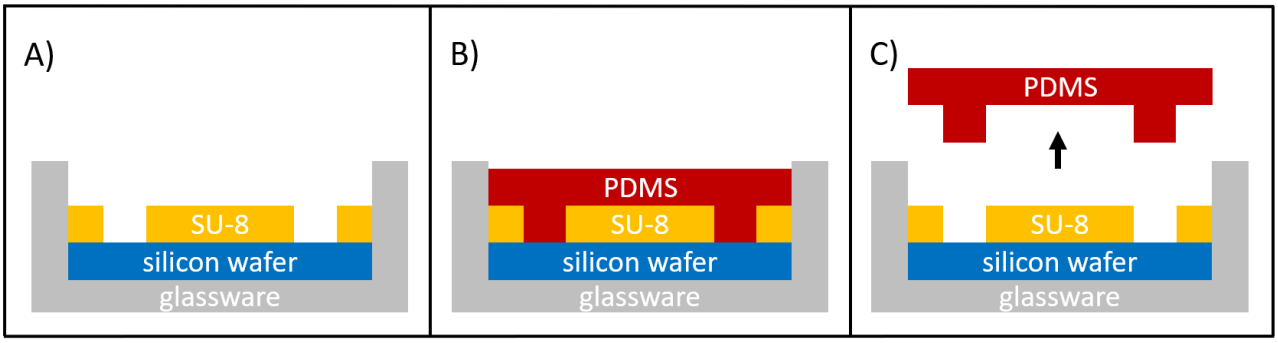

Figure E.1: Side cut of the PDMS stamps fabrication process. A: A patterned silicon wafer is placed in glassware which is few millimeters wider than the wafer. As detailed in appendix F, the substrate has been coated with an anti-stiction layer to ease the unmolding of deep features like the PDMS cylinders. B: A PDMS paste is poured on the substrate, the targeted thickness is 7mm. It consists of a 10:1 mixture of silicon past and curing agent which has been placed in a vacuum bell for 2 hours to remove air bubbles made during the mixing. It is then baked at 70°C for 2 hours. C: the PDMS layer is unmolded and diced.

Appendix F

Fabrication of the stamp's mold

The mold is created by patterning a thick layer of SU-8 2050 on a silicon wafer. This photoresist has a high viscosity. When transferring it into a small bottle, make sure to wait at least 5 hours. This ensure that no more air bubbles are present in the bottle.

1. Clean a silicon wafer with acetone and then IPA and dry the surface with the air gun pointed in the middle for the wafer.
2. Bake the wafer on a hotplate for 5 minutes at 150°C to improve the adhesion of the SU-8 on it.
3. Place the wafer in the spin-coater. Approach the bottle of SU-8 2050 at 2cm from the wafer to prevent the formation of air bubbles. Pour enough photoresist to cover 2/3 of the wafer's surface. Apply the following spinning recipe:
4.

spinning recipe	
seconds	rpm
5	500
10	500
10	1000
25	1000
5	0

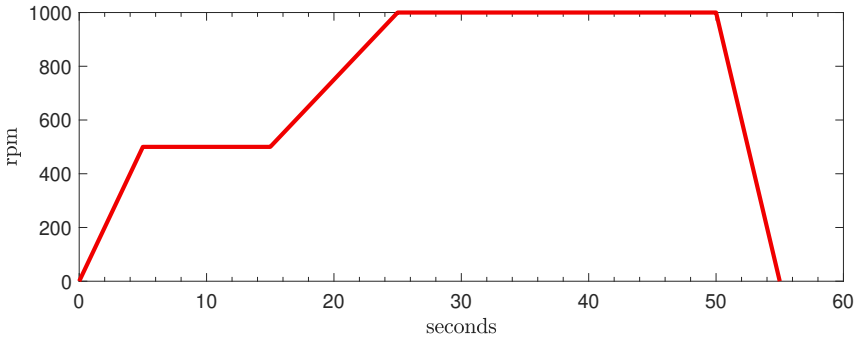

5. Perform the pre-exposure bake on hotplates. Bake the wafer at 65°C for 7 minutes and then at 95°C for 40 minutes.
6. Expose with a dose of 290 mJ/cm^2 at a wavelength of 365nm.
7. Perform the post-exposure bake on hotplates. Bake the wafer at 65°C for 5 minutes and then at 95°C.
8. Develop in glassware filled with 5 mm of MR DEV 600. Place the wafer in the developer for 16 minutes. Move the wafer in the solution to renew the developer at its surface.
9. Place the wafer in IPA for 10 seconds.
10. Renew the developer in the glassware and place the wafer inside for 10 seconds.
11. Repeat this process between one or two times until no more white precipitated liquid is formed.
12. Hard-bake the SU-8 at 180°C for 5 minutes on a hotplate.
13. Ask an experienced operator to place the coated wafer in a vacuum bell with few milliliters of trimethylsilyl chloride for 1 hour. This liquid will create an anti-stiction layer and ease the unmolding of the PDMS.

Appendix G

Alignment setup for the bonding agent transfer

As mentioned in the main text, we transfer the bonding agent by using stamps made silicon polymer (PDMS). In this appendix, we present the setup that was built to manipulate the stamps. It is used to soak the stamp by placing it into contact with a silicon wafer coated with a photoresist, see fig.G.1

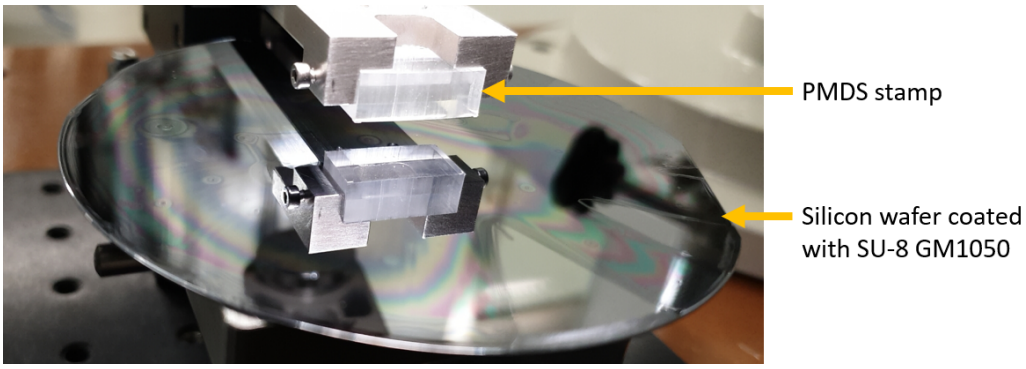

Figure G.1: The first step of the transfer consist of placing the stamp at the surface of an SU-8 spin-coated silicon wafer.

Once the stamp has photoresist on the tip of its cylindrical features, the wafer is removed. A chip is placed inside the clamp and the stamp is placed into contact with it. Fig.G.2 presents the different parts of the setup.

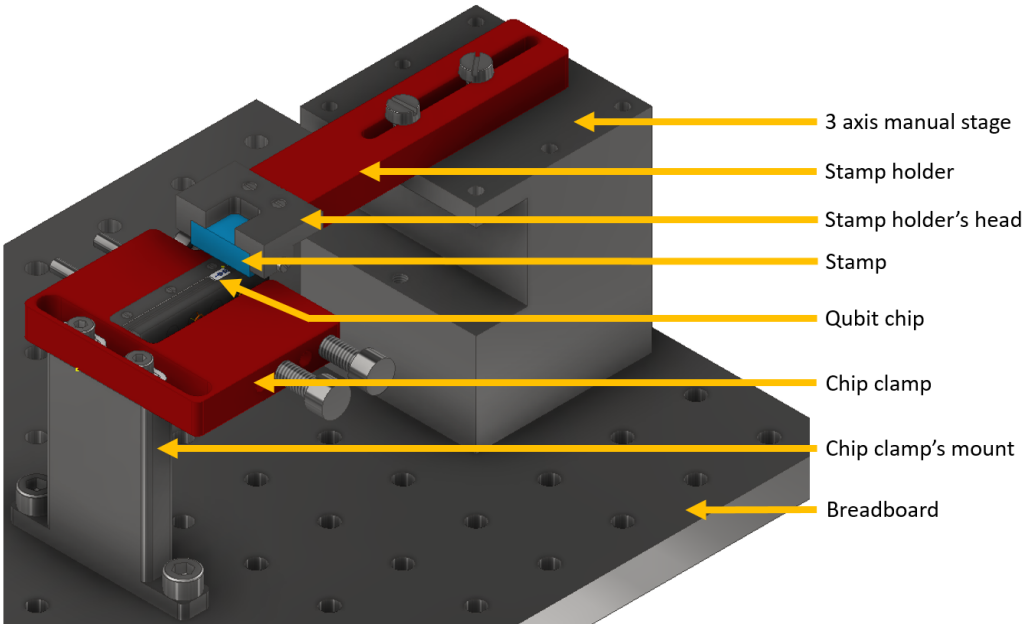

Figure G.2: Inventor rendering of the alignment setup. The chip clamp and the manual stage are screwed on a breadboard to ensure stability.

The alignment setup is designed to be used with a stereo microscope, see fig.G.3. The stamp being

transparent, the operator can see the stamp's cylindrical feature and the qubit chip beneath, see figG.4. The qubit chip has additional marks showing where to place the glue drops.

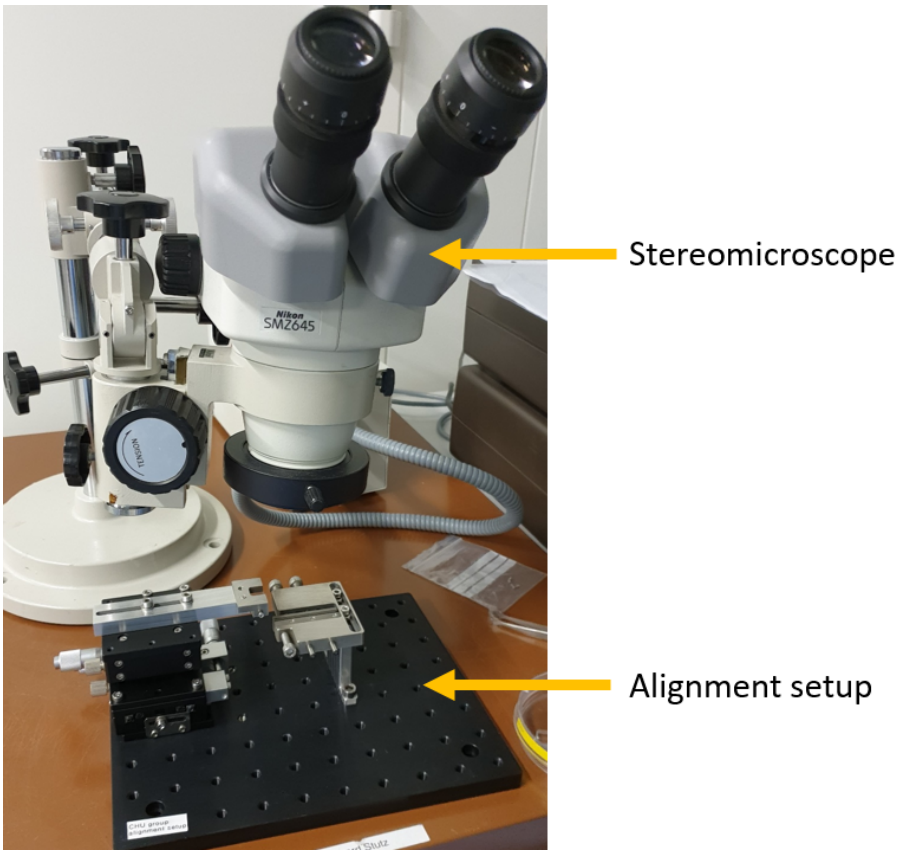

Figure G.3: The stamp alignment setup is used with a stereo microscope.

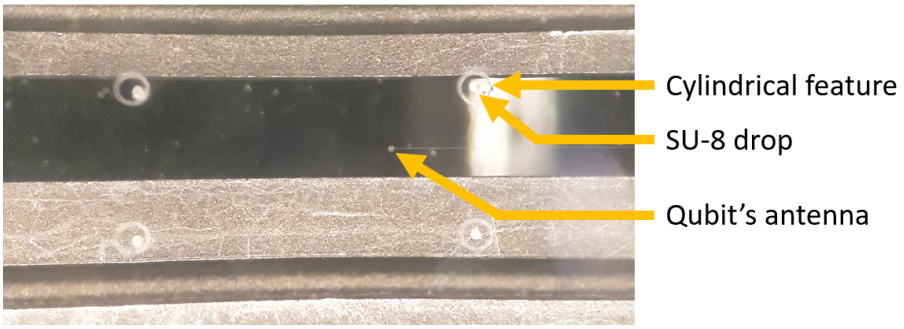

Figure G.4: The top view provided by the stereo microscope gives all the necessary information to the operator the perform the transfer. We can see the cylindrical features and the drops of bonding agent (SU-8) on the tips of the latter.

The stamp is tightened on the stamp holder's head with two screw, see fig.G.5.

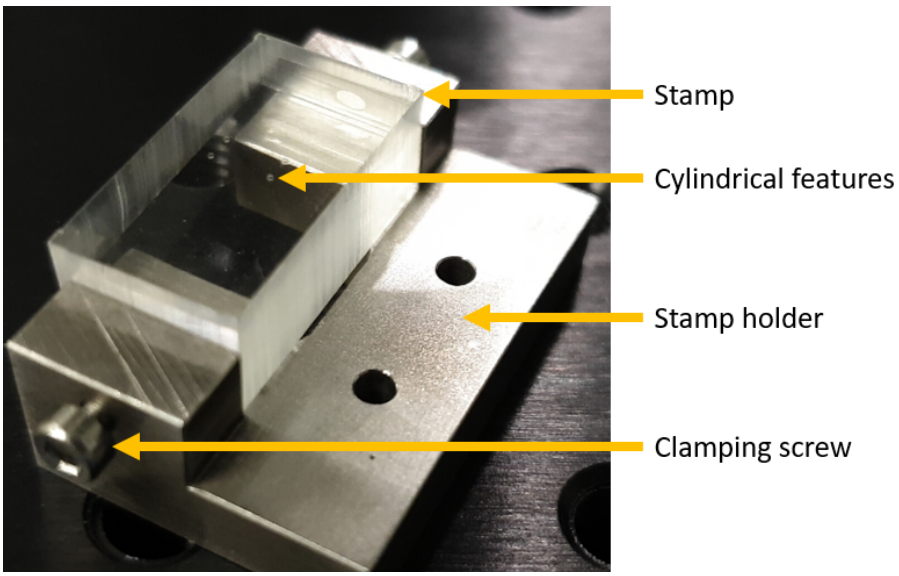

Figure G.5: The stamp is fixed on the stamp holder by two clamping screws.

The stamp holder's head is then screwed on the stamp holder which is mounted on the 3 axis manual stage, see fig.G.6.

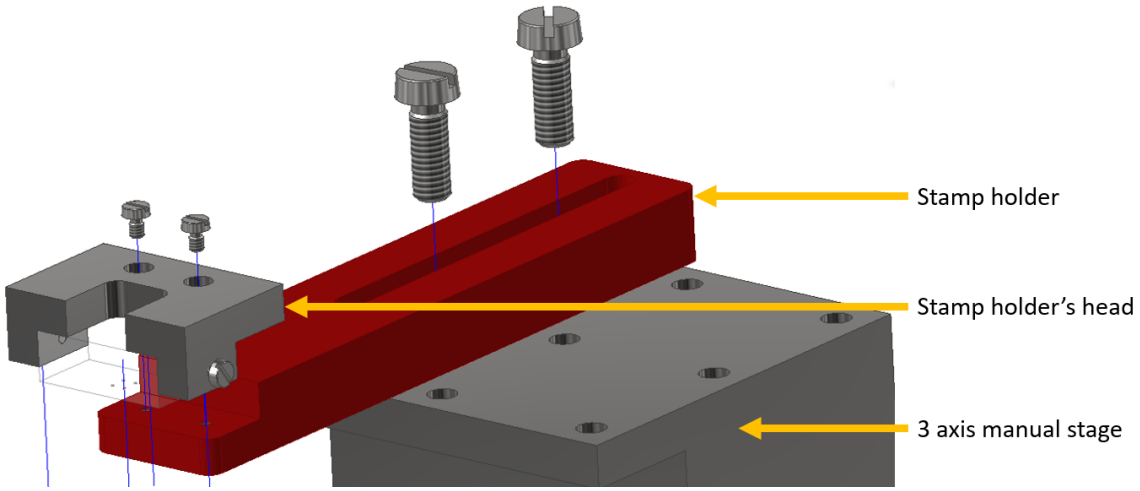

Figure G.6: The stamp holder's head is screwed on the stamp holder which is mounted on the 3 axis manual stage.

The chip holder is made of two clamps. The first is screwed on the chip holder, see fig.G.7.

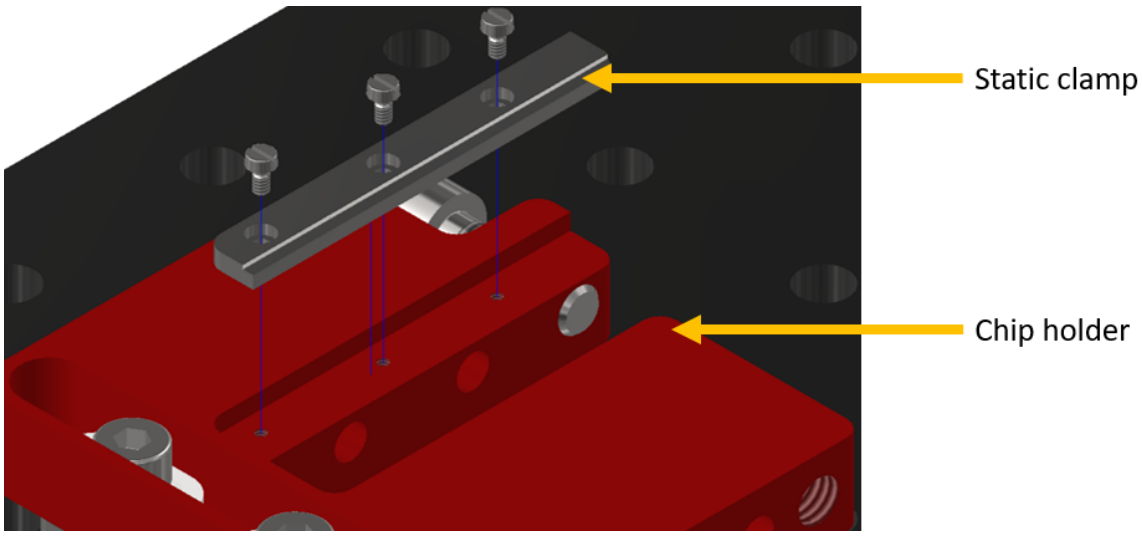

Figure G.7: A clamp is screwed on the chip holder, details about its geometry are given in fig.G.8.

Both clamps are designed to present clamping surfaces inclined towards the chip, see fig.G.8. This particular choice was made to compensate for the roughness of the qubit chip's sides, see fig.3.1.

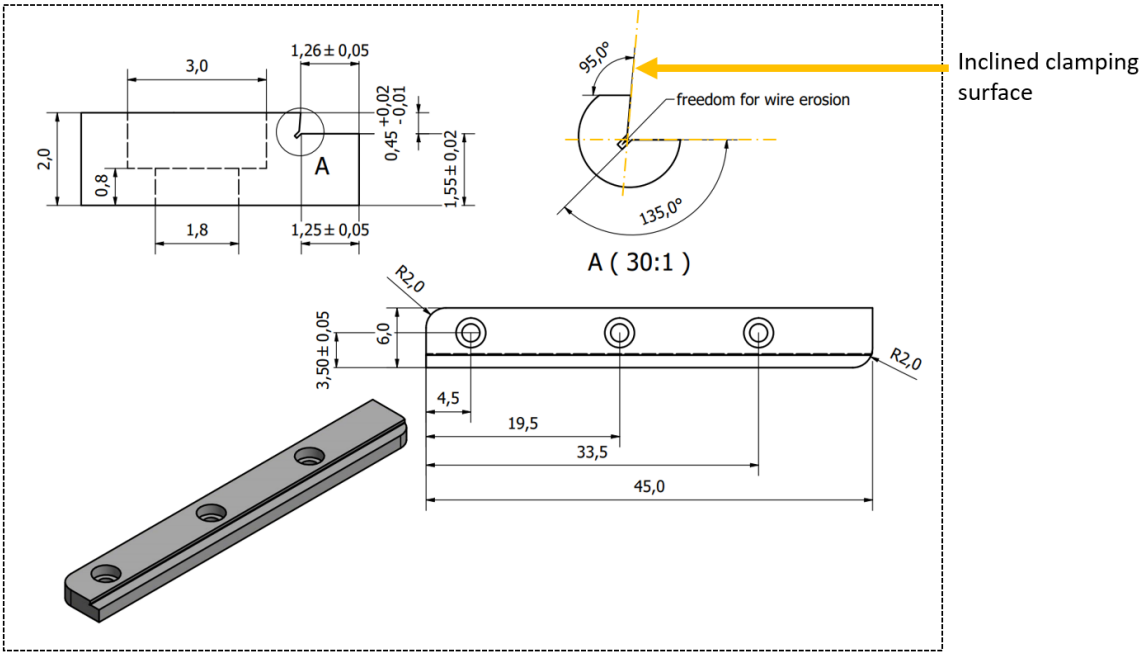

Figure G.8: The technical drawing of the clamp specifies an obtuse angle of 95° between the clamping surface and the upper surface of the clamp. Technical note: wire erosion was used to machine accurately the clamping surface.

The other clamp is guided through the chip holder by two rods. The clamping force can be adjusted by a pair of screws pushing against the guided springs, see fig.G.9.

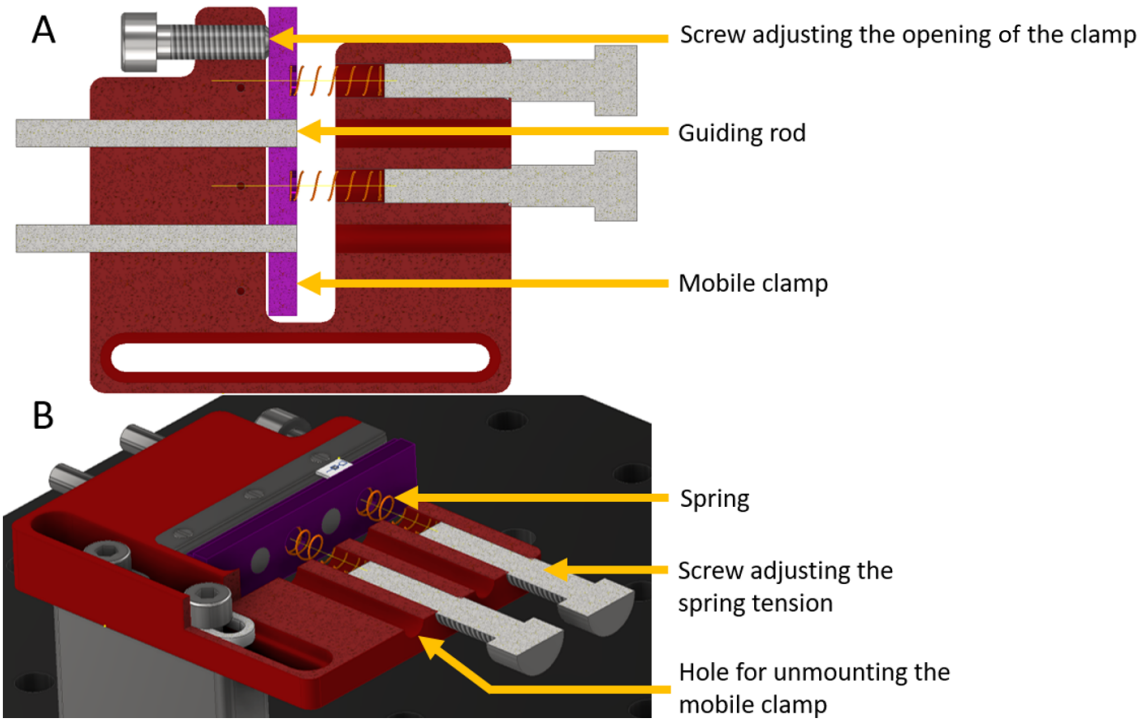

Figure G.9: A: Half-section view of the chip holder. A screw is used to adjust the position of the guided clamp. A pair of guiding rods constrain the mobility of the clamp. B: 3/4-section view of the chip holder. A pair of screws is used to adjust the force that the springs apply on the guided clamp. A pair of holes drilled in the chip holder ease the unmounting of the guided clamp.